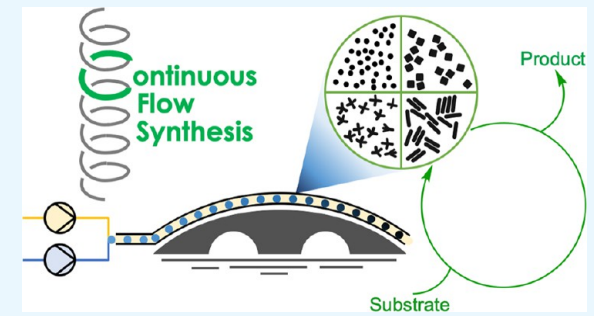


Continuous Flow Methods of Fabricating Catalytically Active Metal **Nanoparticles**

Emily J. Roberts, Lanja R. Karadaghi, Lu Wang, Onah Malmstadt, **, Doah Malmstadt, **, and Richard L. Brutchey*, † 6

ABSTRACT: One of the obstacles preventing the commercialization of colloidal nanoparticle catalysts is the difficulty in fabricating these materials at scale while maintaining a high level of control over their resulting morphologies, and ultimately, their properties. Translation of batch-scale solution nanoparticle syntheses to continuous flow reactors has been identified as one method to address the scaling issue. The superior heat and mass transport afforded by the high surface-area-to-volume ratios of micro- and millifluidic channels allows for high control over reaction conditions and oftentimes results in decreased reaction times, higher yields, and/or more monodisperse size distributions compared to an analogous batch reaction. Furthermore, continuous flow reactors are automatable and have



environmental health and safety benefits, making them practical for commercialization. Herein, a discussion of continuous flow methods, reactor design, and potential challenges is presented. A thorough account of the implementation of these technologies for the fabrication of catalytically active metal nanoparticles is reviewed for hydrogenation, electrocatalysis, and oxidation reactions.

KEYWORDS: continuous flow, nanoparticles, catalysis, microfluidics, millifluidics, nanofabrication

1. INTRODUCTION

Greater than 85% of chemical processes make use of a catalyst, with 80% of industrial catalytic processes utilizing solid heterogeneous catalysts and the global catalyst market being greater than \$20 billion (USD). Therefore, there are strong economic drivers to continue developing catalysts with higher selectivities, activities, and stabilities, which will result in both economic and environmental gains. One direction of catalyst development has been to utilize nanoscale materials, such as nanoparticles, as the active catalyst since these materials often exhibit unique chemical and physical properties compared to their bulk counterparts. The surface-area-to-volume ratios of nanoparticles increase with decreasing particle size, and in the nanoscale size regime, surface properties dominate the overall material behavior. What was once thought of as materialspecific properties, such as melting point and dielectric constant, have been shown to be different for the same materials on the nanoscale. Differences in the size and shape of nanoparticles can yield electronic, optical, and electromagnetic properties that are different from the bulk, and enable the potential for their use in new applications, such as catalysis.^{3–7}

Currently, commercial methods of synthesizing nanoscale catalytic materials consist of traditional precipitation and impregnation methods. Precipitation and co-precipitation utilize a homogeneous solution of the corresponding metal salt, or salts, to achieve a solid catalyst through a three-step process of supersaturation, nucleation, and, then, subsequent crystal growth. Supersaturation can be achieved by physical transformations, such as change in temperature, or chemical reactions, such as the addition of acids or bases.8 In order to achieve small and uniform particles, homogeneously high supersaturation levels are necessary, but because the system naturally evolves toward a decrease of supersaturation through the nucleation of particles, the time scale to achieve these high levels is short as it is limited by mass and heat transport.8 As co-precipitation employs the use of multiple metal salts to achieve multicomponent systems, it can be challenging to achieve the desired phase and/or homogeneous precipitation. The impregnation method affords a supported catalyst by incorporating a metal component into a preformed catalyst support. Two main impregnation techniques are (1) wet impregnation and (2) incipient wetness impregnation. Both methods utilize a solution of the metal precursor in which the support is immersed, with wet impregnation having an excess of solution where the metal diffuses into the support and incipient wetness impregnation using a solution with a volume equal to, or slightly less than, the known pore volume of the support, utilizing capillary action. 11 Regardless of the method,

Received: April 25, 2019 Accepted: July 9, 2019 Published: July 9, 2019



Department of Chemistry, University of Southern California, 840 Downey Way, Los Angeles, California 90089-0744, United States *Mork Family Department of Chemical Engineering and Materials Science, University of Southern California, 925 Bloom Walk, Los Angeles, California 90089-1211, United States

Table 1. Advantages and Disadvantages of Nanoparticle Catalyst Preparation Methods

nanoparticle catalyst preparation method	advantage	disadvantage
current methods (precipitation, impregnation)	widely adopted cost effective	support dependent challenging to obtain high weight loadings in a single step
	scalable	wide distribution of particle sizes and morphologies
colloidal batch methods	excellent control over particle size, size distribution, and morphology	difficult to scale because of heat and mass transport limitations
		safety issues with batch scaling
		batch-to-batch variability
flow fabrication methods	automatable	not widely adopted
	efficient heat and mass transfer	industrial scale out has not been demonstrated
	superior reproducibility	
	reduced environmental health and safety risks	
	higher yields, shorter reaction times	
	control over particle size, size distribution, and morphology	

both resulting supported catalysts require drying and calcination/reduction before use. Another drawback to impregnation methods is that the maximum loading is limited by the adsorption capacity of the support being used.¹

While these techniques are able to provide industrially relevant quantities of catalysts with high surface-area-tovolume ratios, they often fail to result in materials with monomodal size distributions or morphological control that is on par with current solution-phase methods of synthesizing colloidal nanoparticles (Table 1). Over the past few decades, there has been a great deal of effort in investigating and understanding colloidal nanoparticle nucleation and growth processes, ^{12,13} the effect of ligands on particle size and morphology, ^{12,14–18} and compositional control. ^{18–21} This collective body of research has resulted in the ability to rationally design and prepare catalytically active materials with highly tailored sizes, morphologies, and compositions. 15,20,22-25 Exploitation of nanoparticle structure-function relationships is especially useful for catalytic applications, as different nanoparticle morphologies can favor different pathways because of significant differences in reactant binding energies associated with different crystal facets and surface energies.26-30

The existence of a nanoparticle structure—reactivity relationship, with respect to catalytic activity, was clearly exhibited in an example by Narayanan and El-Sayed in which they synthesized Pt nanoparticles with three distinct shapes, tetrahedral, cubic, and nearly spherical particles, which displayed different reactivities for the same electron-transfer reaction.²⁸ This group later correlated the catalytic activity of these Pt nanoparticles with the fraction of surface atoms on the corners and edges, revealing that the tetrahedral shape had the highest reaction rate constant, as well as the highest percentage of atoms on edges and corners compared to those of cubic and nearly spherical Pt nanoparticles.31 Similarly, the shapedependent catalytic activity of Ag nanomaterials was demonstrated to rely heavily on the nature of the exposed crystallographic plane.³² For Ag nanocubes, which display purely (100) facets, the rate of conversion for the oxidation of styrene was over 14 times higher than Ag nanoplates and 4 times higher than Ag nanospheres, which display solely the (111) and both the (111) and (100) facets, respectively. Therefore, the ability to synthesize nanoparticles with discrete

sizes and morphologies can enable a high level of control over the resulting catalytic reactivity for a synthesized colloidal nanoparticle catalyst.

While colloidal nanoparticle catalysts derived from "bottomup" solution-phase syntheses offer distinct advantages over traditionally synthesized nanoscale catalysts, as discussed above, the major drawback of colloidal nanoparticles is that it is nontrivial to synthesize them at an industrially relevant scale (Table 1). Currently, nanoparticle syntheses are performed in batch on bench scale (~10-100 mL), generally producing small amounts of product during each reaction (\sim 25–250 mg). Furthermore, the synthetic conditions under which nanoparticles are fabricated have a colossal effect on the resulting particle size, size distribution, and morphology. The challenge of scaling lies in the fact that nanoparticle nucleation and growth processes are extremely sensitive to heat and mass transport limitations, and as the reactor size or reagent concentration is increased, there is reduced control over the mixing and heating profiles.³³ This lack of control often leads to lower quality materials with wider size distributions and more poorly defined morphologies, which may ultimately lead to non-uniform catalytic properties. Additionally, since batch colloidal nanoparticle chemistries developed at the laboratory scale often utilize corrosive or caustic reagents, undergo exothermic reactions, and result in gas evolution when heated, there are safety risks (and associated costs) related to doing these chemistries at large scale.

In response to the aforementioned challenges, continuous flow techniques have been identified as a robust method to fabricate nanoparticle catalysts (Table 1). Microfluidic and millifluidic reactors afford superior reaction control for the production of large amounts of nanomaterials due to the small dimensions of their channels. Quantitative comparisons of transport phenomena in batch reactors and microfluidic reactors have been addressed with analytical approaches.³⁴ Convective mass and heat transfer dominate in batch reactors. Thorough mixing in batch reactors requires high Reynolds numbers and optimized impeller geometries, and mixing becomes more difficult with increasing volume in the scaleup process. Diffusive mass transfer and conductive heat transfer are dominant in continuous flow reactors. These transfer rates are inversely proportional to the square of the characteristic channel size, making heat and mass transfer in

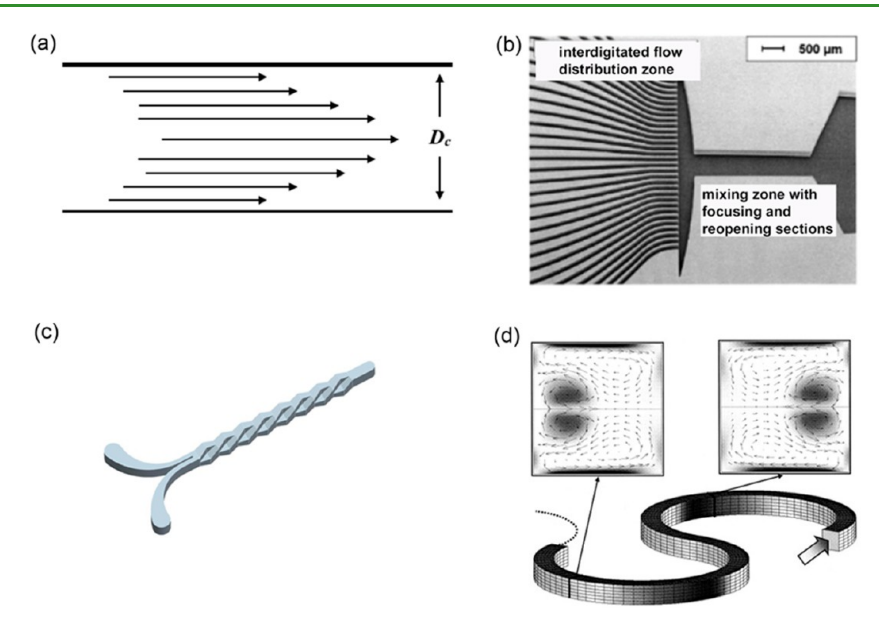


Figure 1. (a) Parabolic velocity profile displayed by laminar flow, where D_c is the inner diameter of the channel. (b) Scanning electron micrograph of a single layer forming a slit-shaped interdigital micromixer. Reprinted with permission from ref 48. Copyright 2003 Wiley-VCH. (c) Schematic of the internal structure of a ramp-like caterpillar micromixer that drives split-and-recombine mixing. Reprinted with permission from ref 50. Copyright 2013 Wiley-VCH. (d) Diagram of a curved channel and cross-sectional views of different circular segments, inducing Dean vortices. The arrows indicate the direction of flow, displaying chaotic flow patterns that ultimately lead to greater mixing within the channel. Reprinted with permission from ref 52. Copyright 2004 Wiley-VCH.

micro- and millifluidic reactors inherently advantageous. The ratio of reaction rate to mass-transfer rate in a reactor is described by the Damköhler number (Da). Da < 1 indicates a kinetically reaction limited system, where mixing is sufficiently fast, while Da > 1 indicates that mixing is limiting and may result in undesired products and lower yield. When batch reactions are scaled, Da increases, but micro- and millifluidic reactors can be scaled (either by increasing run time or by parallelization; see below) without increasing Da.

The superior heat and mass transport stemming from the high surface-area-to-volume ratios of the channels allows these large quantities to be attained without compromising control over their resulting morphology and polydispersity. The improved heat-exchange efficiency can additionally mitigate temperature fluctuations from highly endo- or exothermic reactions, which are prevalent in nanoparticle syntheses. Effective heat transfer and efficient passive mixing also mean that flow-synthesized nanoparticles frequently require shorter reaction times, but exhibit increased yields, compared to the analogous batch reaction. ^{36–39}

What makes continuous flow methods all the more plausible as a solution for the commercialization of colloidal nanoparticle syntheses is the amenability to automation and parallelization. The increased throughput and superior reproducibility that flow methods afford mitigate the aforementioned batch challenges. Furthermore, the miniaturization of solvent and reagent volumes that are at a given temperature at any given time will be smaller than a large tank reactor, affording increased safety. The goal of this review is to provide a concise account of the previous work performed in the field of continuous flow metal nanoparticle catalyst fabrication and provide necessary information for chemists and chemical engineers to consider when making particles in flow.

2. OVERVIEW OF CONTINUOUS FLOW METHODS

2.1. Flow Regimes. The miniaturization of macroscale processes to micro- and milliscale continuous flow reactors results in an increase of the surface-area-to-volume ratio of the channels to the flowing fluids. Decreasing the dimensions of the reactor does not change the fundamental physics of flow from those observed for macroscale fluid dynamics. 40 However, the difference in the surface-area-to-volume ratio influences the type of flow that is achieved in these systems as a result of the increased interaction of the flowing fluid with the channel walls at these smaller length scales. 40 In general, there are two types of flow regimes that can be achieved—laminar and turbulent flow. At the macroscale, mixing is achieved in all directions by irregular and chaotic swirling motions resulting from vortices and flow fluctuations, which is termed turbulent flow. 41 In laminar flow, which is the predominate flow observed for miniaturized systems, two or more fluids flow in streamlined paths parallel to each. The two regimes can be differentiated by the influence of the viscous and inertial forces, with laminar and turbulent flow being achieved when the viscous forces and the inertial forces dominate, respectively. In laminar flow, mixing is purely diffusive, with mixing time inversely proportional to the diffusivities of the species being mixed. 42 Turbulent mixing is more complex to describe, but it is necessarily faster than purely diffusive mixing because it combines molecular diffusion with flow characteristics that both reduce diffusion length and mimic convective mixing. Many passive and active mixing technologies have been developed to increase the rate of mixing in microfluidic systems. 43 As described below, multiphase flows can also be deployed in microfluidic channels to greatly decrease mixing

2.2. Single-Phase Flow. Laminar flow in continuous flow reactors is easily achieved using a simple T- or Y-shaped junction in which two miscible fluids are merged into a single channel and flow parallel to one another, mixing through

diffusion across the interface between the two fluids. The main challenge with synthesizing nanoparticles with laminar flow is the ensemble of nucleation times that result from the parabolic velocity profile of the fluid inside the channel walls (Figure 1a). 44 The parabolic velocity is a result of the fluid velocity at the channel walls being zero due to the no-slip boundary between the fluid and the wall, causing the liquid in the middle of the channel to flow with a faster velocity. 40,45 This can lead to a broadening of the resulting size distribution of particles. Furthermore, diffusive mixing leads to concentration gradients both perpendicular to and along the length of the reactor that can lead to inhomogeneities in reaction conditions. 46 Additionally, the slower velocity of the fluid that interacts with the channel wall can result in fouling during nanoparticle syntheses, which will be discussed in more detail in section 3.1. The time scale in which mixing occurs is directly proportional to the square of the channel diameter and inversely proportional to the diffusivity of the species being mixed.4

Advances to lamination mixers have been implemented to enhance the degree of mixing through increasing the contact surface area of different fluid streams and through novel reactor geometries. 41 Parallel lamination of the fluids into very thin interdigitated streams results in shorter stream interdiffusion distances, thus requiring shorter reactor lengths for mixing (Figure 1b). 47,48 Alternatively, chaotic advection can be achieved through careful design of the reactor architecture by implementing obstacles in the channel path, altering the wall with ridges or grooves, or by altering the reactor channel geometry from a straight line into a zigzag or serpentine pattern, which perturbs the flow and generates a transversal component to the velocity. 49 For example, a micromixer, called the caterpillar mixer, developed by the Institute of Microtechnology Mainz (IMM), used the principle of splitting and recombining in which the two fluids are split into multiple streams (~300) in a channel containing ramp-like structures (Figure 1c).⁵⁰ This structure facilitates subsequent recombination of the two fluid streams in both the horizontal and vertical directions through folding, reorientating, and recombining, resulting in superior mixing compared to typical, straight laminar flow devices. Serpentine architectures induce a secondary flow phenomenon referred to as Dean flow, which arises from vortices occurring from fluid flow in curved channels (Figure 1d). The centrifugal force produced by the reactor curvature causes the fluid in the middle of the channel to be pushed to the outer channel wall, resulting in recirculation of the fluid, mitigating against the stagnant fluid observed near the walls of a straight channel.^{51,52}

2.3. Two-Phase Flow. A significant amount of effort has been directed toward the improvement of mixing in flow reactors by employing multiphase flow. 53-55 Multiphase, or segmented flow, can be achieved for liquid-liquid or liquidgas systems by using two or more immiscible phases to form droplets or plugs of one phase in the other. The reagents makeup the liquid dispersed-phase droplets or plugs that are isolated from one another by a partially or completely immiscible liquid or gas carrier phase. The geometrically confined droplets serve as identical "reactor vessels" with respect to volume and reagent concentration. The continuous phase encapsulates the droplets, isolating them from one another and the channel walls. As the droplet moves downstream, the forces exerted on the sides of the droplet due to contact between the moving droplet and the stationary

channel walls induce two countercirculating flows (Figure 2a). 56 These forces can be further maximized by using a curved

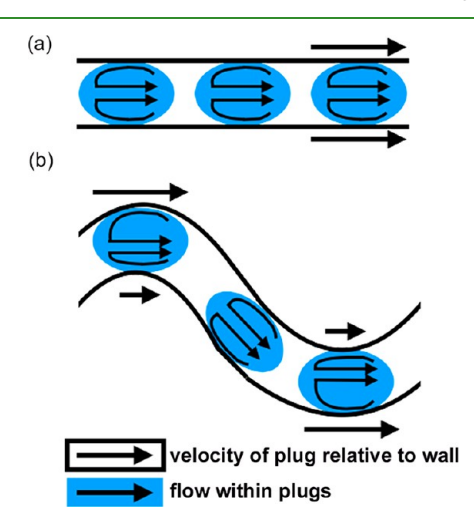


Figure 2. Example of droplets formed in multiphase flow, moving through (a) straight and (b) curved channels. The arrows depict the velocity of the droplet relative to the channel wall, in addition to the position of flow within each droplet. Straight channels produce relatively symmetric countercirculating flow within the droplets, while curved channels produce asymmetric vortices. Adapted with permission from ref 57. Copyright 2004 The Royal Society

channel, facilitating asymmetric vortices which are present in Dean flow, which is discussed further in section 4.1.1 (Figure

The formation of droplets is typically achieved using a flowfocusing device or T-junction. Flow-focusing devices produce droplets by flowing the dispersed phase between two streams of immiscible fluids through a small orifice, causing the continuous phase, which has a higher viscosity, to encapsulate the dispersed phase and form droplets under certain flow rate ratios (Figure 3a). In T-junctions, the dispersed phase is flowed into a junction at 90° to the continuous phase, where the flow of the continuous phase results in a viscous force that, in conjunction with the pressure gradient generated upstream of the junction, breaks apart the dispersed phase into droplets under a certain range of flow rates and flow rate ratios (Figure 3b). 59,60 Multiple-inlet T-junction devices can be used when reagent streams need to be isolated from one another prior to droplet formation, as in the case for nanoparticles that are readily reduced at room temperature. 61 In Figure 3c, this configuration was used for the synthesis of Au and Ag nanoparticles by injecting the metal salt and borohydride reducing agent through inlets 2 and 4, respectively, with an additional solvent stream introduced using inlet 3, creating a barrier between the two to delay diffusive mixing and particle nucleation prior to droplet formation and introduction into the reactor.61

There are a variety of factors that influence the resulting droplet generation using the aforementioned methods such as the interfacial tension of the two phases, wetting properties of the channel walls, the employed flow rates and their respective ratios, and the viscosities of the fluids. 62 In these geometries, droplet formation depends on the ability of the liquid continuous phase to "wet" the inside of the channel; typically good wettability is required for stable droplet formation.⁶ behavior results from the interfacial energies of the solid and

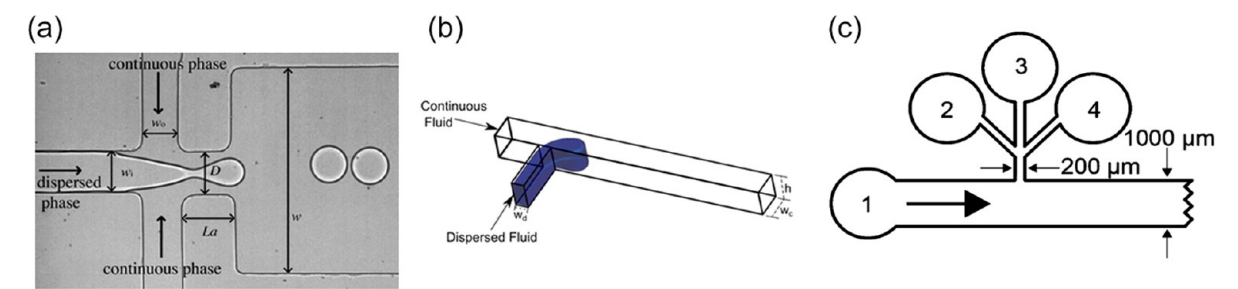


Figure 3. (a) Diagram of droplet formation of a dispersed phase in a continuous phase by flow focusing. The dispersed-phase flows through a channel of width w_i perpendicular to a junction with two continuous-phase inlet channels of width w_0 . The two phases pass through an aperture of width D and length La before droplets are pinched off and dispensed into a collector channel of width w. Reprinted with permission from ref 58. Copyright 2010 The Royal Society of Chemistry. (b) Schematic of a T-junction droplet generator of height h and a continuous-phase channel width of w_c . The dispersed phase is introduced in a channel perpendicular to the continuous phase with a channel width w_d , enabling droplet formation under the certain flow rates and flow rate ratios. Reprinted with permission from ref 60. Copyright 2014 Springer Nature. (c) Diagram of a multiple-inlet T-junction droplet generator. The continuous-phase flows through inlet 1, while reagent solutions are flowed through inlets 2 and 4, separated by a neat solvent stream in inlet 3 to prevent diffusive mixing prior to droplet formation. Reprinted with permission from ref 61. Copyright 2012 American Chemical Society.

the liquid. Consideration must therefore be given during reactor design in terms of solvent choices with respect to the surface properties of the channels, which can be altered by surface coatings for some designs. 64-67 In addition, the interfacial tension, mismatch of viscosities of the two or more phases being employed, and their flow rates have a large influence on the droplet formation process.⁶⁰ While this Review will not cover these topics in depth, extensive information on the influence of these parameters for droplet formation in T-junctions and flow-focusing devices can be found elsewhere; 68-72 in general, the achievable flow rates only facilitate a small range of accessible droplet sizes. The ability to increase droplet size while maintaining high flow rates and flow rate ratios is important, as it is one method of increasing throughput.

Recently, a 3D-printed droplet generator was developed in which a wide range of inlet flow rate ratios and channel surface energies can be utilized with no effect on the droplet diameter (Figure 4).³⁶ This geometry forms droplets by flowing the

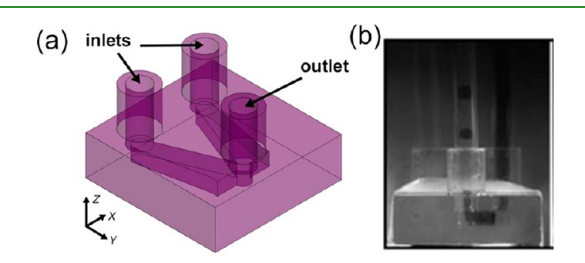


Figure 4. (a) Schematic design of a 3D droplet generator. The continuous and dispersed phases meet at a junction perpendicular to the outlet, where droplets whose size are dictated by the inner diameter of the outlet tubing are formed. (b) Photograph of the 3D droplet generator in operation, showing the formation of droplets of the dispersed phase (black) whose diameter matches the inner diameter of the outlet tubing. Reprinted with permission from ref 36. Copyright 2016 Springer Nature.

continuous and dispersed phases in a perpendicular orientation to the outlet, in which droplets are pinched off and subsequently flow downstream. Unlike in flow-focusing and T-junction devices, the flow rates and geometry of the device do not influence the size of the droplets generated—the droplet size is simply governed by the inner diameter (i.d.) of the outlet tubing, which can be rapidly reconfigured by simply changing the outlet tubing for the same droplet generator (Figure 4). Smart engineering of fluidic components, such as the development of this novel droplet generator, is advancing the feasibility of continuous flow manufacturing.

2.4. Flow Control. The continuous supply of the dispersed and continuous phases can be achieved through a variety of methods. Syringe pumps are the most common method of flow control for micro- and milliscale continuous flow reactors at the laboratory scale. Their simple design consists of a mounted syringe in which the plunger is automatically pushed mechanically to produce a desired flow rate for a predetermined volume of solution, allowing for fast and easy setup and operation. Under ideal conditions, the programmed flow rate will correspond to the actual residence time given a specific length of tubing. However, the actual flow rate often differs from the programmed flow rate due to thermal expansion of the reactor and in situ gas evolution, meaning that the actual flow rate at steady state is unknown without the addition of flow sensors to the system or other methods of quantifying flow. deMello and co-workers demonstrated an automated feedback control scheme that not only corrects the flow rate based on online analysis but also establishes fast optimization on nanoparticle properties synthesized in flow.⁷³ Also, flow rate fluctuations induced by the stepper motor in a syringe pump can be attenuated by adding a buffering side chamber.⁷⁴ However, there are limitations in scale-up with syringe pump. For example, syringe pumps may be subject to stalling resulting from excessive back-pressure from channel clogging. Moreover, their practicality for large-scale operation is restricted due to the limited volume of the syringes that fit into commercially available syringe pumps.

Flow can also be driven by microfabricated pumps. Instead of mechanical motors, these pumps can be actuated by piezoelectric force, electromagnetic force, centrifugal force, or pneumatic force, thereby making their miniaturized design achievable. With their flexible designs capable of manipulating fluid in small volumes, micropumps can precisely deliver liquid, and in multilayer elastic devices where channels can be deflated, a series of valves can serve as a peristaltic micropump.⁷⁵ Micropumps are well-suited for precise liquid and gas control and sufficient micromixing that are critical in nanofabrication in flow; however, their total flow rates are

limited by their small size, reducing their applicability to scaleup applications.⁷⁶

Peristaltic pumps supply fluid to reactors by using a flexible tube that is periodically squeezed to produce a negative pressure that draws solution into the tubing and subsequently releases the fluid, generating a flow. A peristaltic pump is similar to the syringe pump in its ease of setup and operation but with no limit on the volume that can be supplied, which is advantageous for large-scale applications. Additionally, peristaltic pumps are suitable for pumping high-viscosity fluids. One drawback of peristaltic pumps is that their mechanism of pumping induces periodic oscillations, or pulses, in the flow rates, which can potentially negatively influence flow conditions and resulting nanoparticle quality. The chemical resistance and compatibility of peristaltic pump materials should be considered, as many are not compatible with organic solvents. Special fluoroelastomers and silicones have been developed to withstand aggressive chemicals, including inorganic acids and organic solvents.7

It is also common to employ pumps used for highperformance liquid chromatography (HPLC) in continuous flow devices. HPLC pumps are based on a reciprocating, or dual piston, pump design that flows liquid through a one-way check valve. The HPLC pumping rate is governed by a mechanism similar to that of peristaltic pumps, where the piston draws eluent as it retracts and subsequently pumps it through as the piston moves forward. Polyether ether ketone (PEEK) tubing is the main material used in HPLC systems but should not be used with tetrahydrofuran, dimethyl sulfoxide, or methylene chloride.⁸⁰ Additionally, relative to the other methods of inducing flow mentioned, HPLC pumps are capital intensive.

Pressurized systems have been increasingly recognized as a superior method for flowing fluids through reactors due to their ability to achieve stable flows over long run times (i.e., for large fluid volumes). 37,81-83 One advantage of pressurized systems is that there are no pulses produced that can influence the flow rates, as there is no mechanical pumping mechanism.⁸⁴ But, because the reagents are in a relatively open environment, reagent contamination and/or solution evaporation may be problematic in pressure-driven systems. Moreover, corrosive vapor or gas developed may be harmful to the pressure control system and reservoirs, so compatible materials and safety valves are necessary in the pressure-driven system.⁸³ These two problems can be solved by preventing direct contact between the reagent solutions and an open pressure system,⁸⁵ or by using inert, immiscible liquid instead of gas to displace the precursor. Another weakness in this system is that flow rates cannot be directly determined by delivery pressure since it depends on the flow resistance downstream. However, by employing flow sensor feedback, real-time flow rates can be accurately measured and controlled.3

3. POTENTIAL ISSUES WITH SCALING OF NANOPARTICLE CATALYST SYNTHESES BY **CONTINUOUS FLOW**

3.1. Fouling. A major concern regarding commercial implementation of continuous flow methods for nanoparticle catalyst production is the potential for reactors to foul. Fouling is the unwanted buildup of solid material on the channel walls that results in changes in the flow velocity at best and total clogging of the channel at worst. The root cause of fouling is

complicated because numerous factors contribute: the solvents employed, materials being synthesized, the presence or absence of ligands, reagent solubility, type of flow, and the channel material and surface properties, and ultimately the combination of these parameters will be different for all systems.^{86,87} For example, it has been observed that fouling can occur for particulate flows in caterpillar mixers (vide supra) due to the angular nature of the channel walls obstructing flow and resulting in sedimentation.⁸⁸ One would expect this to be a general issue when physical obstructions are used for mixing; however, if the mixer is solely being used for reagent mixing, and nanoparticle nucleation and growth occur downstream, then this becomes less of a problem.

Two main methods that are used in order to generally mitigate against fouling for colloidal nanoparticle syntheses are employment of 3D hydrodynamic flow-focusing or dropletbased flow, and modification of the surface chemistry of the reactor materials. In 3D hydrodynamic flow-focusing, a reagent stream is isolated from the channel walls by focusing it in both the horizontal and vertical directions with either miscible or immiscible liquids.⁸⁹ This can help prevent channel fouling; however, this advantage may be negated by diffusion for nanoparticle fabrication that requires high temperatures and/ or long growth times. As discussed previously, multiphase liquid-liquid droplet-based flow helps prevent the interaction of the dispersed phase with channel walls through encapsulation of the dispersed-phase droplet or plug by an immiscible liquid continuous phase. Without contact with the walls, solids are less likely to be deposited.

Understanding the surface charge or chemistry of the channel wall will also aid in finding solutions to fouling issues. Fouling in a glass channel could occur from a positively charged particle electrostatically interacting with the hydrophilic, negatively charged glass surface (with an isoelectric point of ca. 2.1). 90 Altering the surface chemistry of the glass so that it is no longer hydrophilic is possible, with one option being passivation using self-assembled monolayers through silane reagents. It is important to note that depending on the length, i.d., tubing material, and passivation method, it can be challenging to achieve, and confirm, that a uniform coating is achieved. The thermal, chemical, and lifetime stabilities of the coating also need to be considered for actual use. A nice example by Benyahia and co-workers demonstrates these effects with the fabrication of Au nanoparticles in a 3D glass capillary microfluidic device by the ascorbic acid reduction of HAuCl₄. They showed that at low pH, and with no ancillary ligands present other than ascorbic acid, the glass reactor fouled over the course of minutes (Figure 5).⁹¹ Increasing the pH of the ascorbic acid solution past the isoelectronic point of glass lessens the degree of reactor fouling; however, some degree of fouling is still qualitatively observed in the time frame of minutes. Increasing the pH of the ascorbic acid solution and including a polyvinylpyrrolidone (PVP) capping agent for the resulting Au nanoparticles eliminated reactor fouling completely.

3.2. Gas Evolution. The ability to reproducibly control flow rates allows for the desired residence times to be achieved in continuous flow reactors. Under ideal conditions, the calculated residence time, based on the flow rates and tubing volume, will match the experimentally observed residence time. However, this is not always the case and oftentimes the observed residence times are shorter. In situ gas evolution from gas-evolving reducing agents, decomposition of precursor

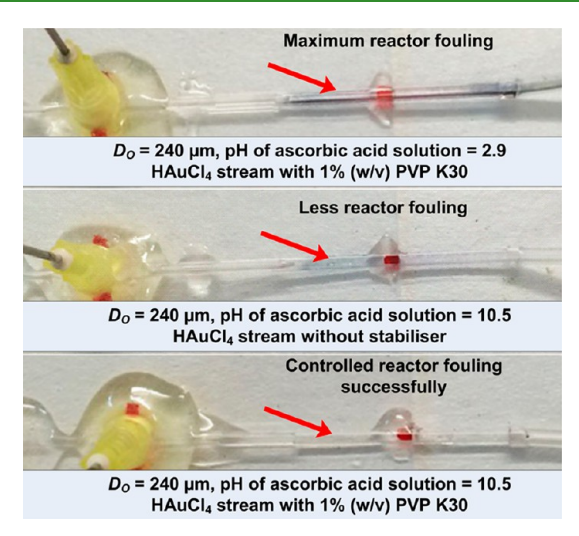


Figure 5. Glass capillary reactor fouling from Au nanoparticle fabrication, as indicated by red arrows. The greatest degree of fouling was observed with an ascorbic acid solution at low pH, followed by an ascorbic acid solution at high pH without the presence of PVP. Fouling was successfully controlled by the combination of a high-pH ascorbic acid solution and the presence of PVP. Reprinted with permission from ref 91. Copyright 2017 Elsevier.

species, or dissolved gases in solvents can decrease the residence time by increasing the flow rates. As gas is evolved in the reactor, it displaces the liquid contents of the channels and, depending on the extent of gas evolution and the liquidphase flow rates, can push reagents back toward the reactor inlet as well as forward to the outlet. If the reagents start to back-flow, reagent reservoirs could potentially be contaminated and/or reactor fouling may occur. To avoid this, continuous debubbler designs based on liquid-gas interfacial tension or selectively permeable membranes can be applied to achieve degassing. 92-94 But in the case where the gas evolved serves as reactant that should not be removed, a one-way check valve that does not allow back-flow can be put in-line after the reactor inlet. Further, it is important to ensure that selectively permeable membranes are compatible with the chemistry and temperature of the reaction in question. A back-pressure regulator, or a pressurized system in general, may also facilitate more controlled flow rates in gas-evolving systems.^{37,95} There have been reports of exploiting gas formation for the in situ creation of a stable two-phase flow for nanoparticle fabrication. 96,97

In one recent example demonstrating the importance of gas management, Corbos and co-workers showed that the aqueous borohydride reduction of H₂PdCl₄ results in significant gas evolution where the gas bubbles accumulate in the reactor channel, leading to fouling in one-phase flow (Figure 6). 98 By switching to a triphasic flow system comprised of the aqueous dispersed phase along with fluorinated oil and nitrogen gas continuous phases, fouling was completely eliminated. It was shown that the inclusion of a continuous gas phase was key for managing gas evolved from the borohydride reduction by acting as a gas sink.

3.3. Parallelization. The translation of colloidal nanoparticle syntheses from batch to continuous flow methods addresses many of the problems associated with the scaling of nanoparticle syntheses. However, single-channel continuous flow devices may not achieve the throughput required for industrial applications. Concern over how to further scale has

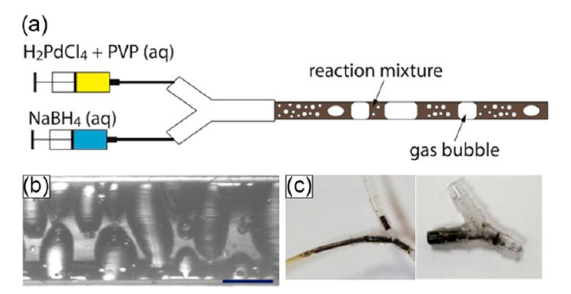


Figure 6. (a) Schematic of one-phase aqueous flow for the fabrication of Pd nanoparticles by the borohydride reduction of H₂PdCl₆. (b) Photograph of reactor channel showing in situ gas formation from the borohydride reduction (scale bar = 0.5 mm). (c) Photographs of Yjunction illustration reactor fouling resulting from gas formation. Reprinted with permission from ref 98. Copyright 2017 The Royal Society of Chemistry.

motivated research into ways of scaling these processes even further. The most straightforward way would be to simply have multiple flow reactors operating simultaneously, which is known as "numbering up". For example, if one reactor system afforded 25 g of material per day, but the required mass of product is 1 kg per day, you would have 40 identical reactors running simultaneously. One drawback to this approach is that operational differences in the equipment driving flow can ultimately lead to product variations, similar to batch reactions. Moreover, numbering up reactors can be capital intensive.

An alternate solution is a reactor that consists of a single set of inlets for the supply of the reagents that can be split into Nchannels for large-scale production of uniform nanoparticles. For example, Foulds et al. developed a poly(methyl methacrylate) (PMMA) droplet generator device that produced liquid-liquid droplets in which N = 512, achieving a flow rate of 1 L h^{-1} for the dispersed phase (Figure 7a). Potential issues in the design of parallelized channels include the potential for one channel to affect a neighboring channel due to inconsistencies in neighboring flow rates or pressure differences, 99 leading to differences in droplet sizes that could ultimately render nanoparticles with various morphologies and polydispersities.

To circumvent the issues with differences in pressure of neighboring channels, the aforementioned flow-invariant 3D droplet generator discussed in section 2.3 was adapted to produce a parallelized system with an N = 4 network (Figure 7b).³⁶ Unlike the previous parallelization example, when operating in the flow-invariant regime, the flow rates or channel pressures do not have an influence on the resulting droplet formation (Figure 7c). This was proven by maintaining a constant continuous-phase flow rate across the channels while varying the dispersed-phase flow rates by using jumper cables with different resistivities. Despite the differences in flow rates, under the flow-invariant regime droplet sizes were consistent across the parallel network and only dependent on the i.d. of the outlet tubing, while operating outside the flowinvariant regime led to droplet sizes that were influenced by the location of their branch in the manifold. While operating within the flow-invariant regime, it was shown that the parallel network could produce Pt nanoparticles where each outlet (A-D) yielded nanoparticles of the same size, within standard deviation.

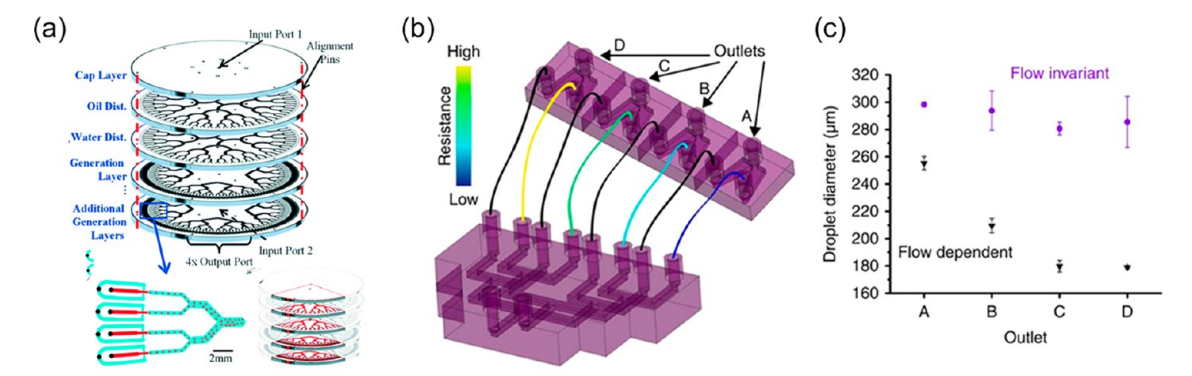


Figure 7. (a) Illustration of a rigid PMMA parallelization chip that stacks four (or more) layers, including a cap layer, oil and water distribution layers, and droplet generating layers. Each droplet generating layer contains 128 flow-focusing droplet generators, as illustrated in the close-up image. Reprinted with permission from ref (99. Copyright 2014 The Royal Society of Chemistry. (b) Schematic of four 3D droplet generators assembled into an N = 4 parallel network that are fed by a distribution manifold. As illustrated, a range of resistances feeding the dispersed phase to the droplet generators is achieved by varying the lengths of jumper cables. (c) Droplet diameters as a function of the droplet generator outlets given in panel b for continuous and dispersed-phase flow rates of 70 and 10 mL h⁻¹, respectively, (purple circles) in the flow-invariant regime and 210 and 30 mL h⁻¹, respectively, (black triangles) in the flow-dependent regime. The flow-invariant region displays control over the droplet diameters in each branch, independent of feed resistance of the continuous phase. Reprinted with permission from ref 36. Copyright 2016 Springer Nature.

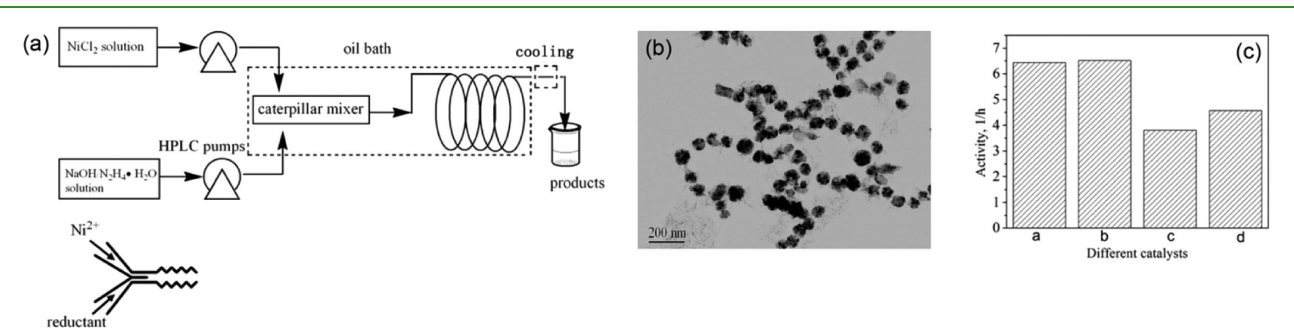


Figure 8. (a) Schematic of the reactor design for one-phase Ni nanoparticle fabrication including the caterpillar mixer. (b) TEM image of ~60 nm Ni nanoparticles fabricated in the presence of CTAB. (c) Activities of Ni nanoparticle catalysts for the hydrogenation of *p*-nitrophenol to *p*-aminophenol [a] without added surfactant, [b] with CTAB, [c] with PVP, and [d] compared to a commercial Raney Ni catalyst. Reprinted with permission from ref 96. Copyright 2012 Elsevier.

4. FLOW SYNTHESIS OF COLLOIDAL NANOPARTICLE CATALYSTS

Catalysts are an integral part of sustaining modern day life as we know it. More than \$10 trillion of the global gross domestic product comes from goods and services that at some point required a catalyst. Catalysts are a key component in the production of chemicals, petroleum refining, food production, emission prevention, and energy generation. The following examples nicely illustrate work done over the past few years in fabricating catalytically active metal nanoparticles in flow.

4.1. Nanofabrication of Hydrogenation Catalysts. Hydrogenation reactions, in which hydrogen is added to an unsaturated bond of an organic compound, are some of the most important in industry. Catalytic hydrogenations typically employ heterogeneous catalysts in a reducing atmosphere created by hydrogen gas.¹⁰¹

4.1.1. Hydrogenation of Nitroaromatic Compounds to Anilines. The transformation of nitroaromatic compounds to anilines is of importance to the fine chemical, agrochemical, and pharmaceutical sectors, and the aniline market as a whole will likely reach \$16 billion USD by 2020. 102 It is estimated that as much as 40–50% of hydrogenation reactions pertain to the reduction of nitro groups. 103 Bayer is one of the largest producers of aniline, in which they utilize a nickel sulfide catalyst for the hydrogenation with a 99% selectivity toward

aniline. ¹⁰⁴ These catalysts are typically prepared using an impregnation method in which $Ni(NO_3)_2$ is supported on alumina, followed by decomposition at 500 °C and subsequent sulfidation by treatment with hydrogen sulfide or carbon disulfide at 450 °C, affording a mixture of Ni_2S_3 and NiS phases. ^{104,105} Other nickel-based catalysts, such as Raney nickel, are commonly used for hydrogenation of nitroaromatics. Additionally, it has been reported that Pd, Pt, and Fe supported on carbon or alumina have high activities and selectivities toward the hydrogenation of nitrobenzene. ^{106,107}

Recently, Zhang et al. demonstrated that catalytically active Ni nanoparticles could be synthesized using a segmented continuous flow method in a microreactor with conventional heating.⁹⁶ The reactor used HPLC pumps to flow two solutions of NiCl₂ and hydrazine hydrate with sodium hydroxide in ethanol into a caterpillar mixer submerged in an oil bath (Figure 8a); in situ gas evolution resulted in twophase, gas-liquid plug flow. The residence time necessary to obtain phase-pure, crystalline Ni nanoparticles was merely 3.9 min, resulting in a throughput of about 11.5 g h⁻¹ of Ni nanoparticles with a mean diameter of 80 nm and a particle size distribution ranging from 60 to 114 nm. Introduction of a cetyltrimethylammonium bromide (CTAB) surfactant reduced the mean size of the Ni nanoparticles to 60 nm with size distribution ranging from 40 to 80 nm. Using PVP as the surfactant resulted in even larger and more polydisperse

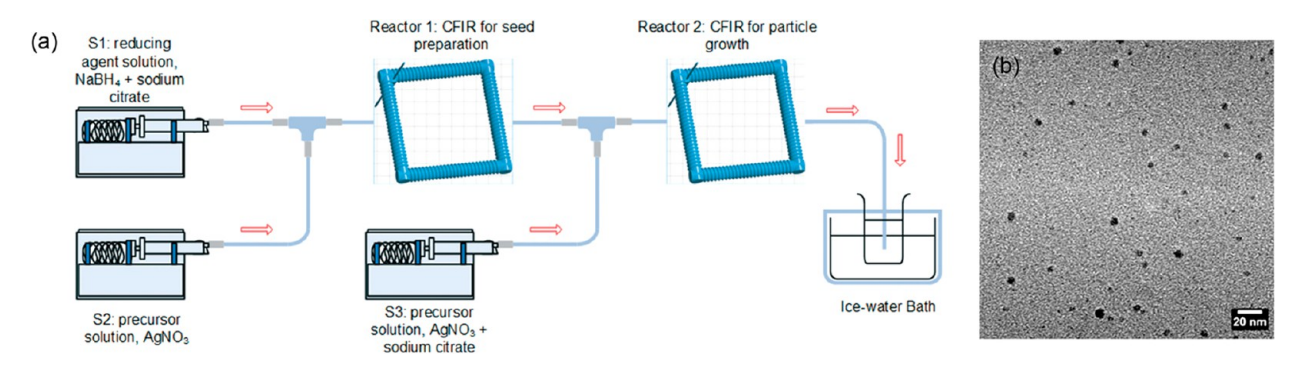
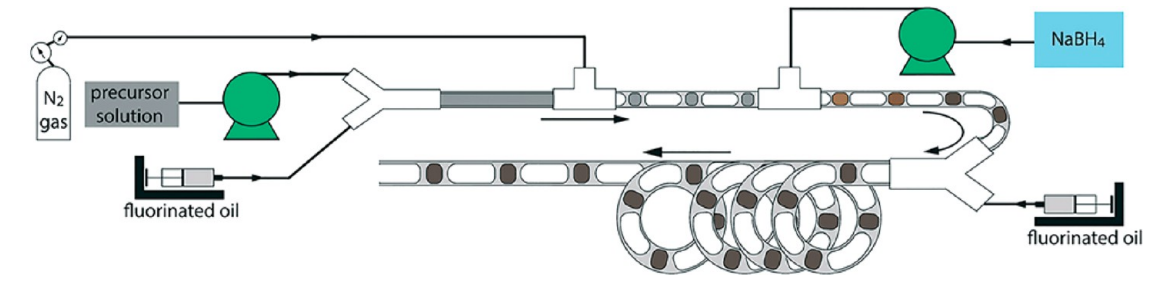


Figure 9. (a) Schematic diagram of the two-stage, one-phase flow reactor for the fabrication of Ag nanoparticles using two coiled flow-inverter reactors (CFIRs) to induce Dean vortices. (b) TEM image of 6.5 nm Ag nanoparticles synthesized in the flow reactor at 60 °C. Reprinted with permission from ref 108. Copyright 2018 The Royal Society of Chemistry.

Scheme 1. Schematic of the Triphasic (Oil, Gas, and Aqueous Phase) Segmented Flow Reactor for Palladium Nanoparticle Synthesis^a



^{ar}The addition of a nitrogen gas phase prevents fouling by acting as a gas sink for bubble formation from the borohydride reduction. Reprinted with permission from ref 98. Copyright 2017 The Royal Society of Chemistry.

particles ranging from 50 to 120 nm. The Ni nanoparticles synthesized with and without CTAB in the flow reactor were then compared to commercially used Raney Ni for the hydrogenation of p-nitrophenol to p-aminophenol, revealing that both the 60 and 80 nm nanoparticles produced in the continuous flow reactor displayed a higher activity than Raney Ni (Figure 8c).

Since noble metals are known to be excellent hydrogenation catalysts, there is interest in exploring noble metal nanoparticle catalysts in order to exploit their high surface-area-to-volume ratios while still achieving the high activity, selectivity, and stability inherent to the metal. Seed-mediated growth methods have been utilized in batch chemistries as a technique to obtain highly uniform nanoparticle morphologies. The same concept can be achieved with continuous flow methods by having reactors positioned in series that can allow for different synthetic conditions to be achieved during sequential steps, such as a different reaction temperatures or chemical environments. This strategy was recently applied to the synthesis of Ag nanoparticles by Torrente-Murciano and coworkers by coiling PFA tubing (i.d. = 0.03 in.) around a 3D-printed support (Figure 9a). This reactor architecture is engineered to promote the rotation of the fluid by the intentional production of secondary Dean flows. The magnitude of Dean vortices can be quantified by the dimensionless Dean number, which is dependent on the hydraulic diameter of the tubing and the radius of the curvature. 52 Interestingly, the Dean number of this reactor displayed a strong correlation to the size and polydispersity of resulting nanoparticles, where higher Dean numbers (>6) tend to result in small (<6 nm) nanoparticles, while lower Dean

numbers yield larger (>8 nm) and much more polydisperse particles. The ability to precisely control the geometric parameters of the reactor, such as helix diameter pitch distance and tubing length, ensures that radial mixing is enhanced as a result of maximization of the Dean number, which facilitates the formation of smaller and more monodisperse nanoparticles. 109

For the synthesis of Ag nanoparticles, two solutions, a reducing agent consisting of sodium borohydride and sodium citrate and an aqueous precursor solution of AgNO3, were flowed through a T-mixer via syringe pumps into the first reactor that was maintained at 60 °C, affording Ag seeds after a residence time of 175 s with an average size of 5.4 ± 1.1 nm. Subsequently, the Ag seeds were flowed through the second reactor stage that facilitated growth at 90 °C by the introduction of additional aqueous AgNO3 and sodium citrate solution via a second T-mixer. The size of the resulting Ag nanoparticles could be controlled by simply adjusting the AgNO₃ concentration in the second step. Five different sized Ag nanoparticles $(6.5 \pm 1.2 \text{ (Figure 9b)}, 6.8 \pm 1.2, 7.7 \pm 1.4,$ 8.0 ± 1.5 , and 9.3 ± 1.8 nm) were synthesized with identical total residence times of 342 s, with the seed and growth steps having residence times of 175 and 167 s, respectively. The highest concentration of Ag solution used in the second step corresponded to a metal throughput of 0.5 mg h⁻¹, assuming complete AgNO₃ conversion. The resulting nanoparticles were tested for the reduction of nitrobenzene to aniline in the presence of excess NaBH4 at room temperature using timedependent ultraviolet-visible absorbance spectra. Contrary to expectation, the catalytic activity did not increase with decreasing particle size. Instead, the optimum size was 6.5 nm, displaying an apparent rate constant of $\sim 900 \times 10^{-5} \text{ s}^{-1}$.

4.1.2. Hydrogenation of Olefins. The hydrogenations of 1-cyclohexene and 1-hexene are commonly used as model reactions for the reactions that occur during hydrotreating, reforming, and fuel processing in the petroleum industry for the upgrading of fuels. Steam-cracked crude oil results in the production of smaller hydrocarbons but contains high levels of aliphatic and aromatic unsaturation. While some olefins are desirable, dienes and alkenylarenes are not, as they can lead to gum polymerization due to their instability. The most commonly employed metals in commercial catalytic hydrogenation of olefins are noble metals, such as Pd, Pt, Rh, and Ru, as well as base metals such as Ni, Co, and Cu. 112

Recently, Pd nanoparticles were synthesized in a singlechannel flow reactor that afforded ~10 L of Pd nanoparticle suspension per day, where the reported Pd precursor concentration and aqueous flow rate equate to >4.5 g of Pd nanoparticles per day, assuming complete precursor conversion.⁹⁸ Here, Corbos and co-workers mitigated against reactor fouling by employing a triphasic segmented flow comprised of oil, gas, and aqueous phases. The flow reactor is configured so that the aqueous H₂PdCl₄ precursor and fluorinated oil are co-injected into a Y-junction using peristaltic pumps, which flow downstream where there are two subsequent T-junctions in which nitrogen gas and aqueous NaBH₄ are introduced into the stream, respectively (Scheme 1). After the introduction of NaBH₄, additional fluorinated oil is injected via a Y-junction and the i.d. of the reactor tubing changes from the milliscale (0.5 mm) to the mesoscale (1.6 mm). This reactor can be thought of as a two-step process, where the milliscale section allows rapid mixing for the nucleation of uniform Pd seeds, followed by subsequent growth in the mesoscale portion, with the first and second stages having residence times of 10 and 80 s, respectively. Operation at the mesoscale facilitates higher throughputs to be achieved while requiring lower pumping pressures.

This work highlights how smart engineering of the reactor can address challenges with the translation of batch chemistries to flow methods. Potential back-flow from hydrogen gas evolution resulting from the decomposition of sodium borohydride was avoided through the incorporation of a nitrogen gas phase, which acted as a gas sink. The fluorinated oil and the nitrogen gas completely isolated the aqueous droplets from the channel walls, mitigating against fouling. Fouling was reported when the gas phase was not included (vide supra). Furthermore, high throughput was achieved by using a mesoscale i.d. tubing for the growth stage, enabling a fast flow rate of 300 mL h⁻¹ for the aqueous phase, which was stable for at least 6 h of run time. Smaller, more monodisperse Pd nanoparticles were achieved in the flow synthesis (2.3 ± 0.3) nm), compared to an analogous batch reaction that was performed on a typical benchtop scale of 10 mL, affording 3.4 \pm 0.9 nm nanoparticles, as seen in the transmission electron microscopy (TEM) images given in Figure 10.

The resulting catalytic activity toward the hydrogenation of 1-hexene was higher for the flow-synthesized Pd nanoparticles (11.9 \pm 0.7 mol_hexane mol_Pd nanoparticles $^{-1}$ s $^{-1}$) compared to the batch-synthesized Pd nanoparticles (6.2 \pm 1.1 mol_hexane mol_Pd nanoparticles $^{-1}$ s $^{-1}$), which can be explained by the increased surface-area-to-volume ratio of the smaller, flow-synthesized nanoparticles. Furthermore, to verify the robustness of this method, samples collected every hour during the 6 h

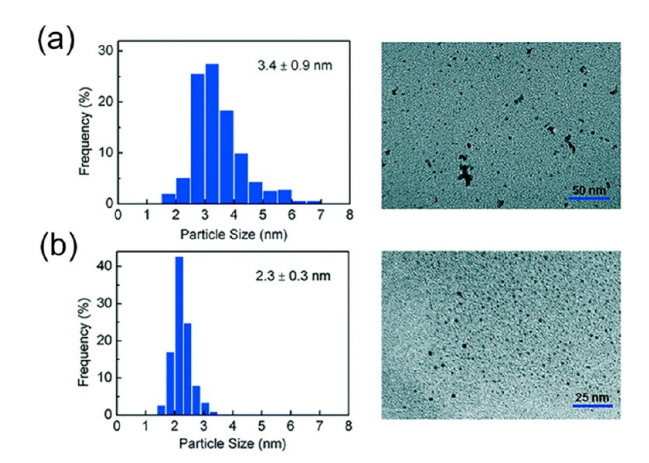


Figure 10. Nanoparticle size distributions and TEM images of the (a) batch-synthesized Pd nanoparticles and (b) flow-synthesized Pd nanoparticles. The flow synthesis yields nanoparticles of smaller mean size and narrower size distribution compared to those fabricated in a small-scale batch reactor. Reprinted with permission from ref 98. Copyright 2017 The Royal Society of Chemistry.

nanoparticle synthesis reactor run were analyzed for both their size and catalytic activity. It was found that the nanoparticle size was consistent across all samples, as well as the catalytic activity by comparison of their turnover frequency (Figure 11).

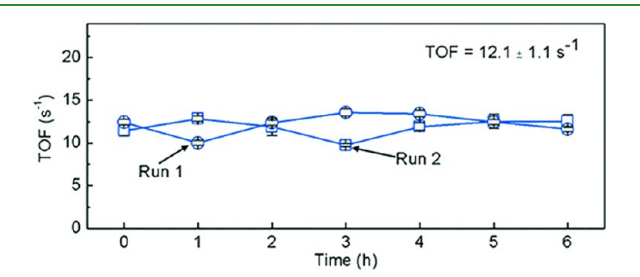


Figure 11. 1-Hexene hydrogenation turnover frequencies of Pd nanoparticle catalysts taken hourly from two distinct nanoparticle fabrication runs, highlighting the Pd nanoparticle production fidelity over a long time interval. Reprinted with permission from ref 98. Copyright 2017 The Royal Society of Chemistry.

While employing the use of multiple phases mitigates against reactor fouling, allows for gas management, and affords superior mixing compared to solely one-phase flow, it has recently been demonstrated that two-phase flow can also provide control over nanoparticle morphology. Multipod structures of Rh nanoparticles were achieved using microwave irradiation coupled with a two-phase millifluidic flow method (Figure 12). A 3D-printed droplet-forming device was employed in which three inlets supplied the dispersed phases of RhCl₃ in ethylene glycol and PVP in ethylene glycol, with a continuous fluorocarbon oil phase; the three streams were flowed using syringe pumps (Figure 12a). After droplets were generated at room temperature, the reaction was thermally triggered by flowing them into a microwave cavity in PTFE tubing (i.d. = 0.79 mm).

The morphology of Rh nanoparticles synthesized with twophase flow was investigated at different temperatures and residence times, revealing that, with lower temperatures and shorter residence times, a higher percentage of the nanoparticles displayed a kinetic multipod morphology, whereas, at

Figure 12. (a) Schematic of the millifluidic reactor showing three syringe pumps driving reagents and carrier oil flow, the 3D droplet generator, and PTFE tubing coil in the microwave cavity. For one-phase flow, a device without the carrier oil inlet was used to mix reagents. (b) TEM image of Rh cuboctahedra produced in one-phase flow at 120 °C with a 9 min residence time (scale bar = 50 nm). The nanoparticle size distribution is given as an inset. (c) TEM image of Rh multipods produced in two-phase flow at 120 °C with a 9 min residence time (scale bar = 50 nm). The ensemble possesses a 94% selectivity for the multipod morphology with an average arm length of 6.75 ± 1.40 nm. Reprinted with permission from ref 113. Copyright 2017 American Chemical Society.

higher temperatures and longer residence times, there was a greater percentage of the thermodynamically favored cuboctahedra structures. The mechanism in which these multipods form is suggested to occur by addition of Rh atoms onto four of the eight triangular (111) faces of the cuboctahedra nuclei, as the PVP ligand likely interacts more strongly with the (100) faces. However, as the temperature and residence time increases, the high-energy multipod appendages undergo etching and subsequent transformation to the thermodynamically favored cuboctahedra. Under no reaction conditions did the analogous one-phase synthesis result in Rh multipods; instead these reactions give the thermodynamically favored cuboctaheral morphology (Figure 12) with sizes ranging from 3.62 ± 0.71 to 3.92 ± 0.75 nm for residence times from 9 to 18 min, respectively. The authors systematically concluded that the kinetic product was obtained using two-phase flow conditions because the fluorinated carrier oil, which is a poor microwave absorber, causes the heat in the droplet phase to rapidly dissipate and allows the kinetic product to be trapped. In order to understand the effect of microwave irradiation on the system for the formation of Rh multipods, the analogous reaction was conducted using conventional heating under otherwise identical reaction conditions of 120 °C and a 9 min residence time. These conditions, which yielded a 94% selectivity toward multipods with microwave irradiation, gave only a 72% selectivity toward multipods under conventional heating. For the Rh multipods synthesized with a residence time of 9 min, the theoretical yield, assuming complete conversion, is >1.3 g of Rh per day.

The resulting Rh multipods synthesized with microwave irradiation and conventional heating were supported on a silica (SiO₂) support and compared to similarly sized cuboctahedra Rh nanoparticles also supported on SiO₂, for their catalytic activity toward the vapor-phase hydrogenation of cyclohexene. Since the Rh multipods display a higher ratio of high-energy corner and edge sites, as well as a higher surface-area-tovolume ratio, it is expected that the multipods will display superior catalytic activities. Indeed, the multipod Rh nanoparticles, regardless of the heating method, displayed higher turnover frequencies (6.5 and 8.5 mol_{cyclohexane} mol_{surface site} s⁻¹ for the microwave heating and conventional heating methods, respectively) than the cuboctahedral Rh nanoparticles $(3.5 \text{ mol}_{\text{cyclohexane}} \text{ mol}_{\text{surface site}}^{-1} \text{ s}^{-1})$ for the hydrogenation of cyclohexene, which are all normalized for Rh

content (Figure 13). The slightly higher turnover frequencies displayed by Rh multipods synthesized with microwave

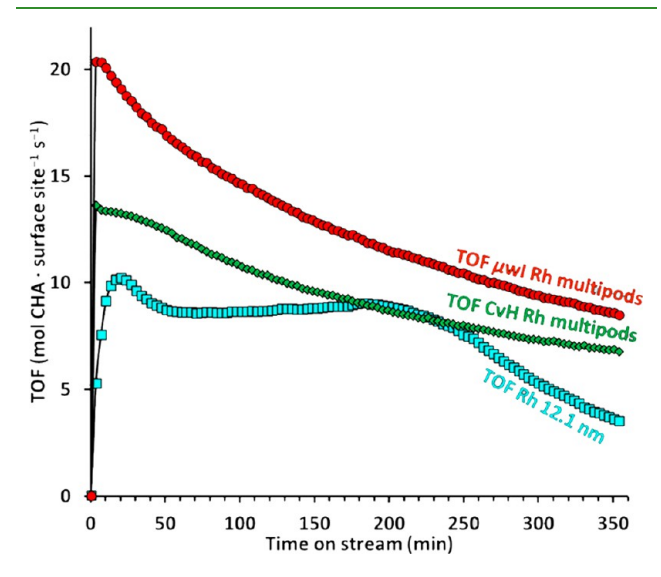


Figure 13. Catalytic activity for the hydrogenation of cyclohexene of Rh multipods synthesized via microwave irradiation (μ wI) and conventional heating (CvH), in terms of turnover frequency, compared to similarly sized Rh cuboctahedra. Reprinted with permission from ref 113. Copyright 2017 American Chemical Society.

irradiation compared to conventional heating matches well to the difference in the population fraction of the catalyst morphologies (i.e., multipods versus cuboctahedra).

Another example of exploiting two-phase flow for control over the resulting nanoparticle morphology has been shown for the synthesis of anistropic, rod-shaped Pd nanoparticles. 95 This high-pressure synthesis (0.8 MPa) was performed using a Pyrex microreactor that was made by traditional lithographic techniques (Figure 12a-c). The reactor chip had a mixing zone, a hot reaction zone, and a cooling zone in which the two solutions, (1) Na₂PdCl₄, KBr, and water and (2) ethylene glycol and PVP, were flowed using syringe pumps at various flow rates to achieve different residence times. A back-pressure regulator achieved a constant pressure of 0.8 MPa for all reactions to control flow rates. Dissolved oxygen in the solvents, as well as the presence of halide anions from KBr, have been reported to influence the morphology of the

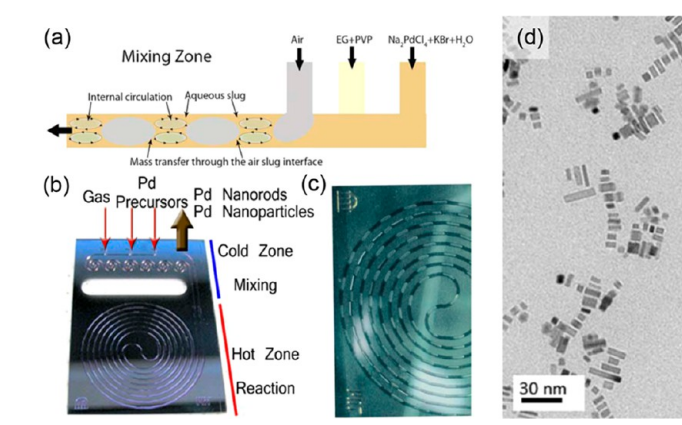


Figure 14. (a) Schematic of two-phase air—liquid flow generation from a T-junction in a microfluidic reactor. (b) Photograph of complete microreactor used for the fabrication of Pd nanorods. (c) Photograph of two-phase air—liquid flow in spiral microreactor. (d) TEM image of Pd nanorods produced in two-phase flow at 160 °C with a 120 s residence time. Reprinted with permission from ref 95. Copyright 2016 Wiley-VCH.

resulting nanoparticles. 114,115 For one-phase flow, a combination of flow rates, achieving residence times from 10 to 120 s, and temperatures, from 160 to 190 °C, were used to controllably tune the morphology from isotropic nanoparticles to anisotropic nanorods. At lower temperatures, the rates of the halide addition to the Pd nanoparticles are comparable to the rate of the oxidative etching, so preferential growth is not observed. However, at elevated temperatures, such as 160 °C, and a residence time of 120 s, the rate of halide ion is faster than the etching, affording nanorods.

To investigate the extent of influence the oxidative environment had on the resulting nanoparticle morphology, a two-phase approach using air as the carrier phase was also employed. In the presence of air, introduced by a T-junction to yield segmented flow, the resulting morphology was exclusively nanorods (Figure 14d), and interestingly, by changing the ratio of Na₂PdCl₄ to ethylene glycol, the aspect ratio (ratio of width to length) of the nanorods could be controlled. At higher ratios of ethylene glycol to Na₂PdCl₄, the aspect ratio was higher. The resulting Pd nanorods were investigated for their catalytic activity toward the hydrogenation of styrene, and the activity was compared to a commercial Pd/C catalyst, performed in the liquid phase using a Parr reactor. Under the same catalytic testing conditions (i.e., 0.1 mM Pd, 0.2 MPa H₂ pressure, 40 °C, DMF solvent), the flow-synthesized Pd nanorods exhibited a 100% conversion of styrene to ethylbenzene within 8 min, compared to 30 min with the commercial catalyst (Figure 15). Additionally, the turnover frequency was substantially higher for the Pd nanorods (6297 h⁻¹), compared to the commercial Pd/C catalyst (1542 h^{-1}).

4.2. Nanofabrication of Electrocatalysts. Fuel cells are promising clean-energy converting devices capable of generating electricity using a fuel source, such as hydrogen, alcohols, and hydrogen-rich hydrocarbons, with the main byproducts being water and heat for hydrogen fuel cells, and water, heat, and CO₂ for hydrocarbon fuel-based systems. The prototypical hydrogen fuel cell is comprised of a proton-exchange membrane (PEM), electrolyte, electrodes, and hydrogen and oxygen as fuel and oxidant, respectively. At the anode, the hydrogen fuel is catalytically split into protons and electrons, followed by the migration of both the protons through the PEM and the electrons through an external circuit to the cathode. At the cathode, the oxygen reduction reaction (ORR) occurs in which the protons and electrons react with

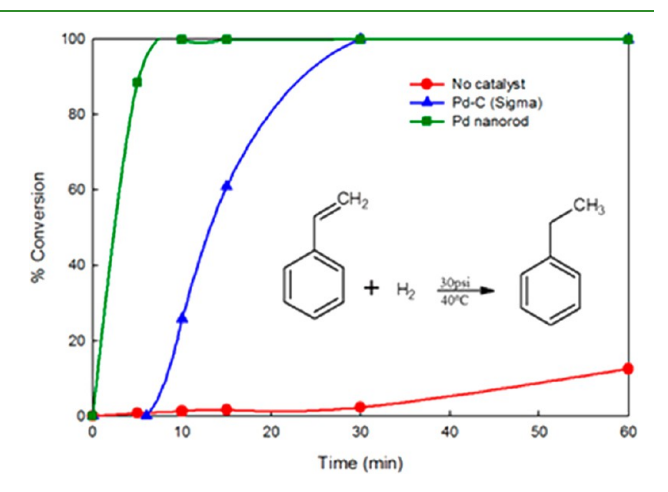


Figure 15. Plot of conversion of styrene to ethylbenzene versus reaction time (min) in the presence of the flow-synthesized Pd nanorods, a commercial Pd/C catalyst, and no catalyst. Catalytic reactions were performed at 0.2 MPa $\rm H_2$ pressure and 313 K. Reprinted with permission from ref 95. Copyright 2016 Wiley-VCH.

oxygen molecules, from the air, to produce water. 117 Hydrogen fuel can be replaced with liquid fuels, such as methanol and ethanol, forming a direct methanol fuel cell (DMFC) and direct ethanol fuel cell (DEFC), respectively, in which protons and electrons are generated in their respective oxidation reactions with an additional byproduct of ${\rm CO_2}^{116}$

The large-scale implementation of fuel cell technology is limited by two major challenges: (1) cost and (2) stability. 117 Both of these issues stem from the Pt-based catalysts that are used to facilitate both the anodic and cathodic electrochemical reactions. Employment of nanoscale Pt for both electrochemical reactions has facilitated the reduction in Pt loading over the past decade, from $\sim\!\!4$ to $\sim\!\!0.6$ mg cm $^{-2}$ in a fuel cell. 116 However, since Pt is a scarce metal, in order for there to be a significant increase in the scale of which fuel cells are produced currently, the amount of Pt needs to be further reduced by approximately 5-fold by alloying with base metals and/or nanostructuring, and a method for the large-scale production of these alternative catalysts needs to be developed. $^{116,118-121}$ Additionally, under the reaction conditions that are typical of fuel cells, Pt is sensitive to contaminants, such as CO, which can result in catalyst poisoning. 122 Therefore, developing methods to facilitate the

large-scale production of superior catalysts in terms of activity, stability, and cost is paramount.

4.2.1. Oxygen Reduction Reaction. One method to reduce the amount of Pt used in catalysts is to incorporate a less expensive, more earth-abundant metal, such as a transition metal that can also result in an enhancement of the specific activity. 123 Xia and co-workers published work with a twophase, continuous-flow reactor for the production of Pt-Ni octahedra. 97 The Pt-Ni octahedra were synthesized using a solution of Pt(acac)2, Ni(acac)2, and W(CO)6 in oleic acid, oleylamine, and benzyl ether that was first heated to 70 °C to dissolve W(CO)₆ prior to introduction into the reactor. Immediately upon entering the reactor, which was heated to 230 °C using an oil bath, W(CO)₆ decomposes, evolving CO gas. The CO gas acts both as a continuous phase, by separating the dispersed phase into discrete droplets that are uniformly spaced, and as a reducing agent (Figure 16). This reaction

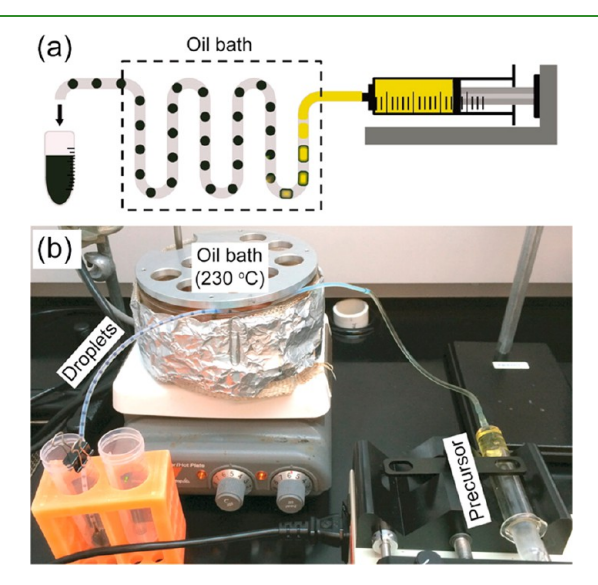


Figure 16. (a) Diagram of a two-phase flow reactor where in situ gas formation occurs from thermally triggered W(CO)₆ decomposition that segments the liquid phase into well-defined droplets. (b) Photograph of the entire PTFE reactor setup, where the tubing enters an oil bath to thermally trigger the reaction and generate gas. Reprinted with permission from ref 97. Copyright 2016 American Chemical Society.

temperature does not facilitate the alloying of W and Pt, so W is not incorporated into the final material. The fluidic device was constructed using a syringe pump that was connected to PTFE tubing with an i.d. = 1.58 mm, which could be changed to tubing with an i.d. = 3.0 mm, to achieve throughput of 20 and 160 mg h⁻¹ of unsupported 9 nm Pt_{2.4}Ni octahedra, respectively.

The use of W(CO)₆ has been previously reported in the batch synthesis of Pt nanoparticles to ensure that uniform morphologies are achieved, because the CO promotes growth of the (111) facet of the octahedra, resulting in Pt nanocubes exclusively displaying (100) facets. 124 At higher concentrations of W(CO)6, more CO gas was evolved, which disrupted formation of the droplets and resulted in Pt-Ni nanoparticles with poorly defined morphologies (Figure 17). Alternatively, lower concentrations of W(CO)₆ result in less CO gas evolution, causing the dispersed phase to flow in plugs, producing Pt-Ni octahedra with larger size distributions.

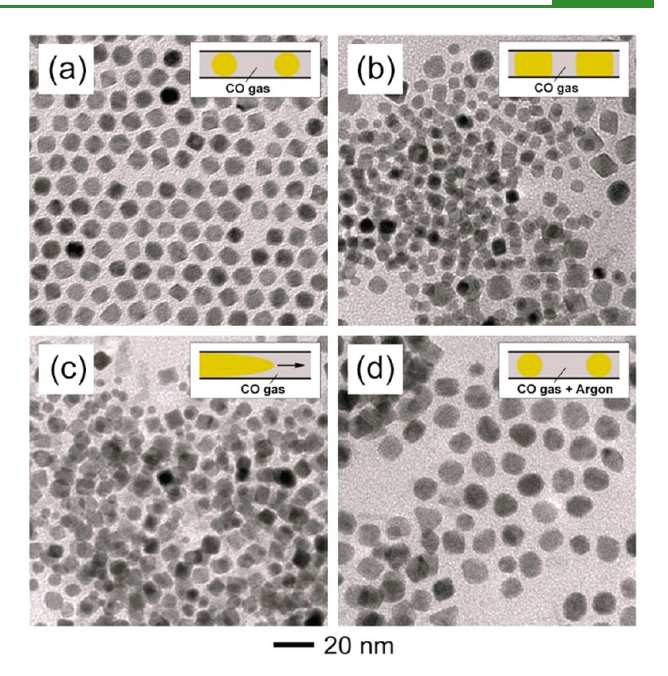


Figure 17. TEM images of Pt-Ni nanoparticles obtained in twophase droplet flow by the addition of W(CO)₆ into the precursor solution at concentrations of (a) 2.0, (b) 1.0, and (c) 5.0 mg mL⁻¹, each resulting in different flow behavior as depicted in the insets. Jetting occurs when W(CO)₆ is used at the highest concentration of 5.0 mg mL⁻¹, while plug formation occurs when $W(CO)_6$ is used at the lowest concentration of 1.0 mg mL⁻¹. (d) TEM image of Pt-Ni nanoparticles formed when Ar was used as the gas phase in the absence of $W(CO)_6$. Reprinted with permission from ref 97. Copyright 2016 American Chemical Society.

Therefore, there was an empirically determined optimum W(CO)₆ concentration in flow that facilitates the in situ formation of well-behaved droplets. Compositional control using this reactor design is achievable by simply adjusting the amount of Ni(acac)₂ in the dispersed phase, affording both 9 nm Pt_{1.7}Ni and 9 nm Pt_{3.0}Ni octahedra.

The 9 nm Pt2.4Ni octahedra underwent an acetic acid treatment to remove surfactants from the surface before being supported on high surface area carbon support (Pt_{2.4}Ni/C) and compared against a commercial Pt/C catalyst. Using a rotating disc electrode (RDE) technique, the electrochemical active surface areas (EASAs) were calculated from hydrogen absorption and desorption, with the Pt2.4Ni/C catalyst exhibiting a smaller EASA than the commercial Pt/C (i.e., 46.4 and 69.4 m 2 $g_{\rm pt}^{-1}$, respectively) from the cyclic voltammograms recorded at room temperature in a N_2 saturated 0.1 M HClO₄ solution. However, the specific activity was much higher for the Pt2.4Ni/C catalyst, giving a current density of 5.74 mA cm⁻² at 0.9 V, whereas the commercial Pt/ C catalyst gave only 0.34 mA cm⁻² at the same potential. The specific activities were calculated by analyzing the ORR polarization curves which were obtained in a room temperature O2-saturated HClO4 solution. The flow-synthesized catalysts were also more stable, with a drop in EASA of 7.7% after 5,000 cycles, compared to a 47% loss for the commercial Pt/C catalyst.

The same group that synthesized the aforementioned Pt_{2.4}Ni/C catalyst also studied the two-phase flow synthesis of multiply twinned Pd icosahedra shelled with a few monolayers of Pt. 125 Instead of in situ gas evolution from a reagent, air was employed as the carrier phase in this report.

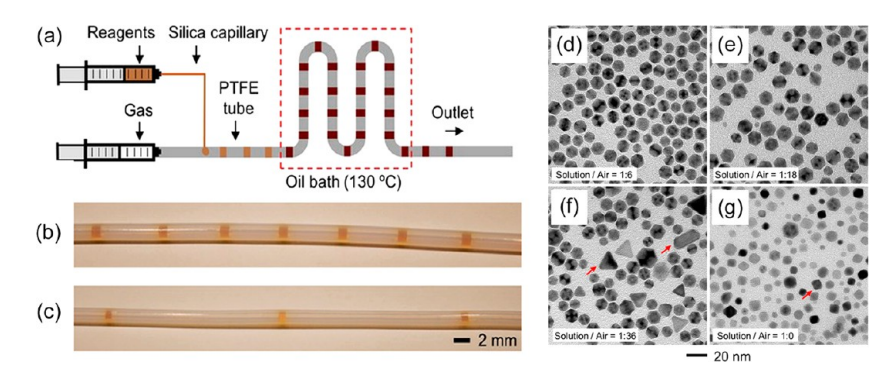


Figure 18. (a) Illustration of the two-phase (liquid—air) flow reactor for the fabrication of Pd nanoparticles, where plugs are formed at a T-junction. Photographs of the PTFE plug reactors containing the reagent solution (yellow) and air (colorless) with (b) 1:6 and (c) 1:36 length ratios between the two phases. TEM images of the icosahedral Pd nanoparticles prepared using (d) 1:6, (e) 1:18, (f) 1:39, and (g) 1:0 length ratios between the reagent solution and the air phase, with arrows pointing out the particles that do not possess the icosahedral shape. Reprinted with permission from ref 125. Copyright 2016 Wiley-VCH.

The dispersed phase was comprised of $\mathrm{Na_2PdCl_4}$ and PVP dissolved in diethylene glycol and introduced via a T-junction. A syringe pump was used to flow both the gas and liquid reagent phases into the reactor that was constructed of PTFE tubing (i.d. = 1.58 mm; length = 7 m) and maintained at 130 °C by an oil bath (Figure 18a). The Pd icosahedra were synthesized with an average diameter of 12.4 \pm 1.2 nm using a tailored ratio of dispersed phase to continuous phase of 1:6, which calculates to approximately a 1.6 mM solution segment, or plug, with a volume of 3 μ L. The influence of this ratio was probed, revealing poorly defined morphologies at higher and lower ratios (i.e., 1:0 and 1:36). At a slightly higher ratio of 1:18 for dispersed phase to continuous phase, the reactor produced the desired icosahedra with 99% purity and a slightly larger average diameter of 14 nm (Figure 18e).

The reason for this morphology control to give well-defined icosahedra is attributed the use of air as the continuous phase, as it has previously been reported to have dual purpose—one being that O2 can serve as an oxidant, generating aldehydes in the polyol reaction that act as the actual reducing agent, and also that the oxidative etching with O2 can alter the reaction kinetics through the oxidation of Pd⁰ back into its ionic form. 126-128 This was proven by performing two control reactions, (1) a synthesis using one-phase flow and (2) substitution of the air continuous phase with pure O2. In both cases, the percentage of icosahedra was reduced significantly, with the former case exhibiting a reduction of the icosahedra population to 15%, whereas with pure O2, with a ratio of dispersed phase to O₂ of 1:12, a population with only 60% icosahedra was produced. This suggests that there is a careful balance between the amount of oxidative species to precursor solution that needs to be empirically determined in order to obtain the highly twinned icosahedra morphology in flow.

The Pd icosahedra were then employed as a substrate to deposit a few monolayers of a Pt shell (Pd@Pt_{2-3L}) in batch. This strategy allows a reduction in the amount of Pt used for catalysis but also has been shown to enhance the catalytic activity toward the ORR for batch-synthesized Pd of various morphologies by adding a Pt monolayer. ^{129,130} The highly uniform shells of Pt were achieved in a batch reaction by the slow (4.0 mL h⁻¹), controlled addition of a Na₂PtCl₆ in ethylene glycol to a solution of the flow-prepared Pd icosahedra in the presence of KBr, PVP, and absorbic acid in ethylene glycol at 200 °C. The reaction was allowed to stir at temperature for 1 h.

The RDE technique was employed to analyze the activity of the Pd@Pt_{2-3L} nanoparticles for their activity toward ORR by supporting the nanoparticles onto Ketjen black carbon to obtain 20 wt % metal catalyst (Pd@Pt_{2-3L}/C) and was compared to a commercial 20 wt % Pt/C catalyst consisting of 2.3 nm Pt nanoparticles. In this case, the normalized EASAs, calculated from the cyclic voltammograms in Figure 19a, were higher for Pd@Pt_{2-3L}/C nanoparticles (100.3 m² g_{Pt}⁻¹) than the commercial Pt/C (52.6 m² g_{Pt}⁻¹), despite the smaller average particle size of the commercial catalyst. The ORR polarization curves were measured in an O₂-saturated aqueous HClO₄ solution, revealing that the mass activities at 0.9 V were

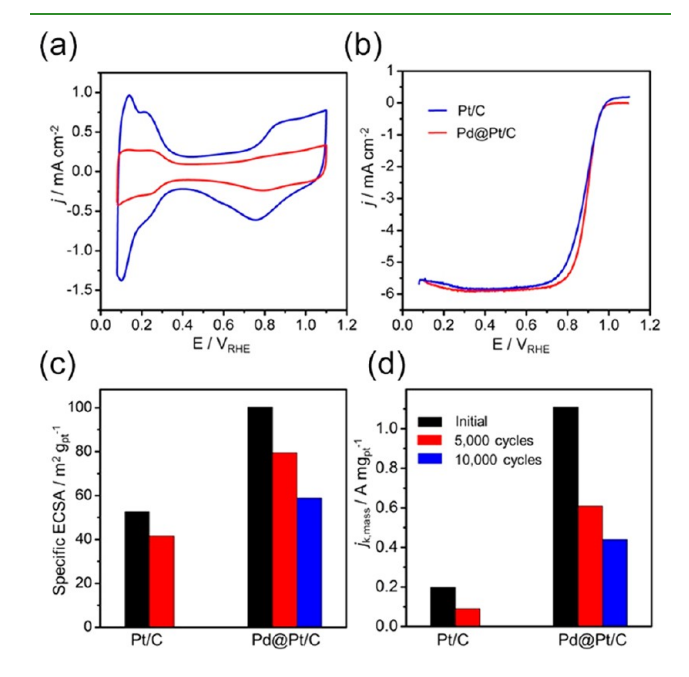


Figure 19. (a) Cyclic voltammograms of the prepared Pd@Pt_{2-3L}/C catalyst and a commercial Pt/C catalyst, and their (b) ORR polarization curves using the RDE method, with current densities normalized to the geometric area of the RDE. (c) Specific ECSAs and (d) mass activities at 0.9 V (versus RHE) for the prepared Pd@Pt_{2-3L}/C catalyst and a commercial Pt/C catalyst before (initial) and after accelerated testing. Even after 10,000 cycles, the specific mass activity of the Pd@Pt_{2-3L}/C catalyst is more than double that of the pristine, commercial Pt/C catalyst. Reprinted with permission from ref 125. Copyright 2016 Wiley-VCH.

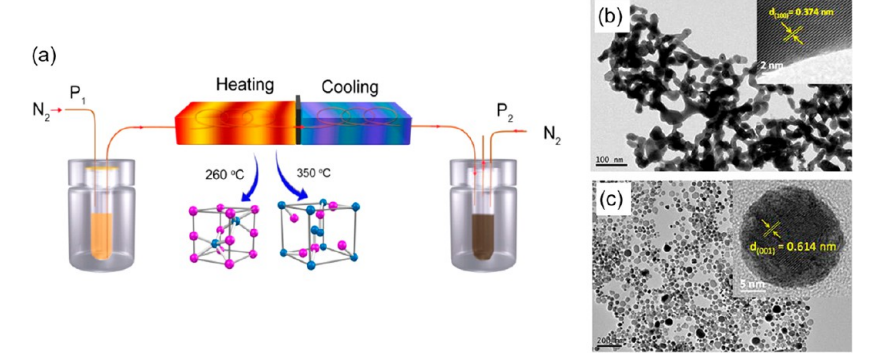


Figure 20. (a) Diagram of the back-pressure-regulated capillary microfluidic reactor system for the fabrication of Pt–Bi nanoparticles. A "heating" zone, where the temperature dictates the phase and morphology of nanoparticles, is followed downstream by a "cooling" zone to quench the reaction. TEM images of (b) Pt₁Bi₁ nanoparticles fabricated at 260 °C displaying a V-shaped nanorod morphology and (c) Pt₁Bi₂ nanoparticles fabricated at 350 °C displaying a quasi-spherical morphology. Reprinted with permission from ref 81. Copyright 2015 American Chemical Society.

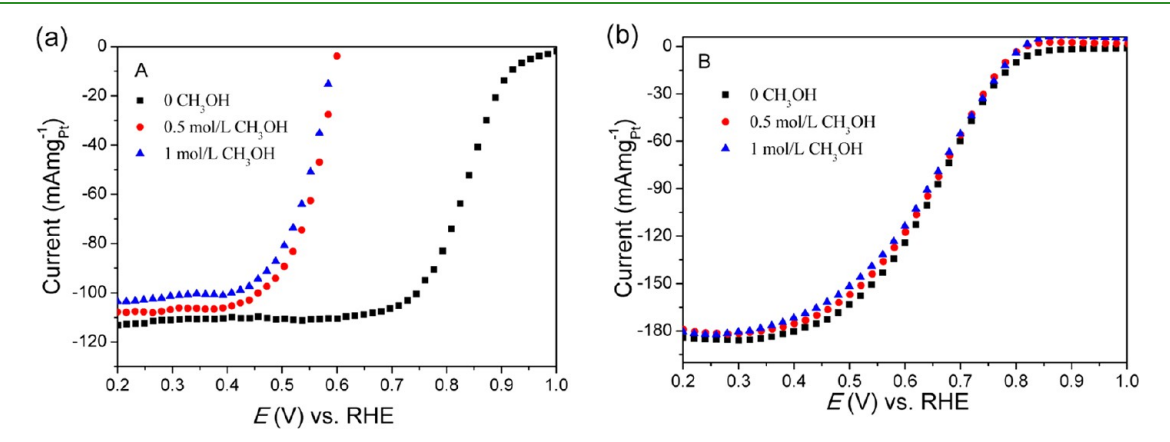


Figure 21. Polarization curves for ORR using (a) commercial Pt/C catalyst and (b) $Pt_1Bi_2/XC-72$ catalyst, with varying degrees of methanol addition. Reprinted with permission from ref 81. Copyright 2015 American Chemical Society.

five times higher for the $Pd@Pt_{2-3L}/C$ nanoparticles (Figure 19b,c). Furthermore, accelerated durability tests were conducted in which the $Pd@Pt_{2-3L}/C$ nanoparticles were shown to have a higher mass activity than the benchmark catalyst even after 10,000 cycles (Figure 19d). While the $Pd@Pt_{2-3L}/C$ nanoparticles displayed high activity and stability toward the ORR, a combination of flow and batch synthetic steps were needed to achieve the final catalyst. Therefore, it would be of great interest to demonstrate that flow methods can be employed for the multistep deposition of a few monolayers of Pt onto a seed Pd particle.

Some of the most promising Pt intermetallics are Pt₁Bi₁ and Pt₁Bi₂ because of their high catalytic activity and stability for ORR, but these materials are more challenging to make than purely noble metal catalysts because their preparation typically requires high temperatures and/or pressures that make it challenging to produce uniform, small, and pure Pt-Bi intermetallics. Recently, Guo and co-workers developed an innovative one-phase flow reactor to circumvent the aforementioned issues for Pt-Bi intermetallic syntheses.⁸¹ The back-pressure-regulated capillary microfluidic reactor utilized nitrogen gas to drive solutions into the reactor that first went through a heated section and then a subsequent cooling section (Figure 20a). The high pressure allowed gasification of the solvents to be suppressed at high temperatures. Using the same precursor solutions of H₂PtCl₆ and Bi(NO₃)₃ dissolved in ethylene glycol, phase-pure Pt₁Bi₁ and Pt₁Bi₂ can both be produced by simply adjusting the

temperature from 260 to 360 °C for Pt_1Bi_1 and Pt_1Bi_2 , respectively, under otherwise analogous conditions. TEM analysis of the final products revealed that the Pt_1Bi_1 exhibited a V-shaped nanorod morphology that made up an extended network, with a rod width of ~17 nm (Figure 20b). Pt_1Bi_2 exhibited a quasi-spherical nanoparticle structure with an average diameter of 33.5 nm (Figure 20c). However, since these particles were larger than the reported desired size of nanoparticles (<3.5 nm) for use as fuel cell catalysts, 131 methods to produce smaller Pt_1Bi_2 nanoparticles were explored.

To synthesize smaller Pt₁Bi₂ nanoparticles, various molecular weight poly(ethylene glycols) (PEGs) were explored, such as PEG400 and PEG600. TEM analysis of the resulting nanoparticles revealed that the particle size correlated to the molecular weight of the polyols used, with PEG600 and PEG400 achieving ~13.2 and ~19.2 nm Pt₁Bi₂ nanoparticles, respectively. The 13.2 nm Pt₁Bi₂ nanoparticles were subsequently investigated for their electrocatalytic performance toward the ORR, because the Pt₁Bi₂ phase is comprised of less Pt than the Pt₁Bi₁ phase. Since methanol crossover in fuel cells can occur, the ORR reaction activity was investigated in the presence of varying amounts of methanol. Polarization curves were obtained using the RDE technique for the supported flow-synthesized Pt₁Bi₂ nanoparticles on Vulcan XC-72 carbon (Pt₁Bi₂/XC-72) and compared to a commercial 20 wt % Pt/C catalyst in an O2-saturated 0.1 M HClO4 solution. A pretreatment process was employed by potential cycling of

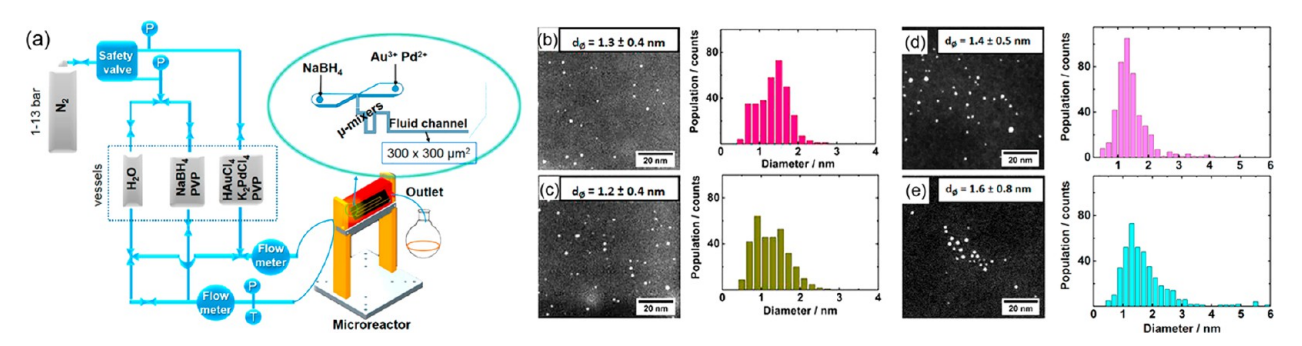


Figure 22. (a) Schematic of the pressure-driven microreactor with cyclone micromixers for the fabrication of AuPd nanoparticles in continuous flow (P and T = pressure transducer and temperature sensor, respectively). (b, c) TEM image and corresponding size distribution of Au_7Pd_3 and Au₃Pd₇ nanoparticles, respectively, produced in flow. (d, e) TEM image and corresponding size distribution of Au₇Pd₃ and Au₃Pd₇ nanoparticles, respectively, produced in an analogous batch reaction. Reprinted with permission from ref 82. Copyright 2018 American Chemical Society.

all electrodes between 0 and 1.2 V versus RHE at a sweep rate of 200 mV/s for 20 cycles in order to clean the surface of the catalysts. As seen in Figure 21, the onset potential and current density displayed in the ORR polarization curves were substantially lower for the commercial Pt catalyst in the presence of any methanol, whereas the flow-synthesized Pt₁Bi₂/XC-72 catalyst remained stable even in the presence of the highest concentration of methanol. The difference in activity and tolerance to methanol is hypothesized to result from the difference in the Pt-Pt (0.474 nm) distance of the Pt₁Bi₂ material compared to Pt-Pt (0.278 nm) in Pt and the difference in charge distribution of the bimetallic structure, both of which influence reaction pathways that would prevent the oxidation of methanol.

4.3. Nanofabrication of Oxidation Catalysts. 4.3.1. CO Oxidation. Historically, CO oxidation catalysts have been of vital importance as they mitigate against pollution resulting from exhaust gas. More recently, concern over purity of fuels for use in fuel cells has motivated the development of efficient CO oxidation catalysts for the production of extremely pure fuel gases, such as H₂, because CO is a poison for many of the catalysts that are used in fuel cells. 132

Ultrasmall AuPd nanoparticles for use as CO oxidation catalysts were synthesized under one-phase continuous flow reaction conditions.⁸² A flow reactor was utilized in which the corrosion resistant stainless steel vessels were pressurized to deliver the reactants with a total flow rate of 2.6 L h⁻¹(Figure 22a), where, depending on the composition, the throughput of this system is ~24-46 g of metal catalyst per day, assuming complete conversion. The two precursor solutions consisting of (1) aqueous HAuCl₄, K₂PdCl₄, and PVP and (2) aqueous NaBH₄ and PVP allowed for Au, Au₇Pd₃, Au₅Pd₅, Au₃Pd₇, and Pd nanoparticles to be synthesized by simply changing the metal salt ratios while maintaining a constant precursor concentration. Rapid and homogeneous mixing was achieved by three cyclone micromixers that are integrated into the microfluidic chip, which is fabricated out of silicon-bonded glass with a 300 \times 300 μ m² cross-section. The high flow rates (1.3 L h⁻¹ for each stream) enabled turbulent mixing to be achieved within 2 ms and only required a 20 ms residence time before being stirred in an off-chip iced round-bottom flask for 1 h for production of the desired Au-Pd, Au, and Pd nanoparticles. The continuous flow synthesized Au₇Pd₃ and Au_3Pd_7 were smaller and more monodisperse (1.3 \pm 0.4 and 1.2 ± 0.4 nm, respectively) than the analogous batchsynthesized nanoparticles (1.4 \pm 0.5 and 1.6 \pm 0.8 nm, respectively), as seen in Figure 22b-e. The enhanced mixing

achieved from the cyclone micromixers in flow facilitated a more homogeneous nucleation process compared to the batch reactor, ultimately achieving nanoparticles with a narrower size distribution.

The resulting nanoparticles were supported on TiO₂ powder to achieve a 1 wt % total metal loading and were subsequently calcinated at 380 °C prior to testing of their activity toward CO oxidation. Investigation into the effect of this procedure on the morphology of the nanoparticles revealed an increase in average diameters of the Au₇Pd₃ and Au₃Pd₇ nanoparticles to 5.3 and 7.3 nm, respectively. The catalytic oxidation of CO was studied using a fixed-bed quartz flow reactor under temperature-programmed mode using temperatures between 30 and 250 °C with catalysts that were pretreated in a reducing atmosphere (5% H₂ in N₂) at 250 °C for 1 h prior to testing. The pure Au/TiO₂ nanoparticles exhibited the typical 20% CO conversion observed at ambient temperature that increased with increasing temperature, reaching full conversion at 120 °C. An increase in Pd content reduced the activity of the catalysts at ambient temperature but resulted in a lower temperature necessary to result in 100% conversion, being ca. 95, 100, and 88 °C for Au₇Pd₃, Au₅Pd₅, and Au₃Pd₇, respectively. The same trend observed for conversion was exhibited by the turnover frequencies being Au/TiO₂ > $Au_7Pd_3/TiO_2 > Au_3Pd_7/TiO_2 \ge Au_5Pd_5/TiO_2 > Pd/TiO_2$.

4.3.2. Oxidation of Benzyl Alcohols. The oxidation of benzyl alcohols to benzaldehydes is of importance because derivatives of benzaldehydes are often used as intermediates in the agricultural industry for the production of pesticides, the pharmaceutical industry for production of drugs, textile industry for the production of dyes, food industry for almond and cherry flavoring, and the perfume industry as an intermediate for many scents. 133-136

Tsukuda and co-workers investigated the effect of the size of Au nanoclusters on their catalytic activity toward aerobic alcohol oxidation reactions. 137 In order to synthesize small (1– 2 nm) Au nanoparticles with a narrow size distribution that facilitates the elucidation of the effect of small size differences on catalytic activity, extremely fast and homogeneous mixing is necessary. A one-phase parallel lamination device made out of Hastelloy C-276, a nickel-molybdenum-chromium superalloy with an addition of tungsten designed to have excellent corrosion resistance in reducing environments, was used. 138 Syringe pumps supplied the two aqueous solutions of (1) HAuCl₄/PVP and (2) NaBH₄/PVP, which were laminated into 16 substreams each, with a stream thickness of <100 μ m, and then interdigitated with one another (Figure 23a). The 32

Figure 23. (a) Diagram of the one-phase laminar flow micromixer used for the fabrication of Au clusters. (b) TEM image and size distribution of Au clusters prepared in flow. Adapted with permission from ref 137. Copyright 2008 American Chemical Society.

parallel streams were further compressed from a channel width of 3.2 to 0.5 mm to minimize the diffusion length.

The flow synthesis with the highest precursor solution concentration using the highest flow rate resulted in the smallest average Au cluster size (Figure 23b) based on TEM and optical absorption, affording a throughput of ~4.7 g of Au nanoparticles per day assuming complete precursor conversion. These Au clusters were then compared to a previously reported Au cluster batch synthesis using similar conditions. 139 Typically TEM analysis would be sufficient in determining the size differences between reactions: however; since these clusters are quite small (<2 nm), the resolution of the TEM does not provide accurate data to facilitate quantitative comparison because there is limited spatial resolution (~0.2 nm). Therefore, the flow- and batch-synthesized Au clusters were compared using a battery of characterization techniques. The flow clusters were determined to be smaller and more quantized than the batch as confirmed by the optical spectrum displaying a structured profile without a surface plasmon band, whereas the batch reaction did display a surface plasmon resonance. The X-ray absorption fine structure spectroscopy revealed a smaller Au-Au coordination number and bond distance of 4.0 \pm 0.8 and 2.75 Å than those of the batch reaction, which were 6.0 ± 1.3 and 2.78 Å, respectively. Moreover, the diffraction patterns display a single broad peak for both methods that suggested lattice spacings of 2.28 and 2.26 Å and crystallite sizes of 0.9 and 1.0 nm for flow- and batch-synthesized Au clusters, respectively.

The flow- and batch-synthesized Au clusters were evaluated for their catalytic activity toward the aerobic oxidation of phydroxylbenzyl alcohol (Figure 24a). The reaction was performed in a temperature-controlled personal synthesizer under air, in which the p-hydroxylbenzyl alcohol substrate and potassium carbonate were added to water in a test tube. A solution (1 mM in 5 mL of H₂O) of the catalyst was then added that contained identical concentrations of Au and PVP. The conversion of p-hydroxylbenzyl alcohol to p-hydroxylbenzaldehdye at 300 K was determined by gas chromatography over 6 h with the flow- and batch-synthesized Au clusters resulting in isolated yields of 95 and 88%, respectively (Figure 24b). The rate constant for the flow-synthesized Au clusters $(k_{\rm m} = 0.58)$ was 50% higher than that of the batch-synthesized Au clusters ($k_{\rm m}=0.38$). The enhancement in rate constant cannot be simply attributed to the difference in surface area as the size of the flow-synthesized Au clusters determined by powder X-ray diffraction is only 10% greater in surface area. Therefore, Tsukuda and co-workers attribute this catalytic improvement to be a result of the smaller size (different Au-

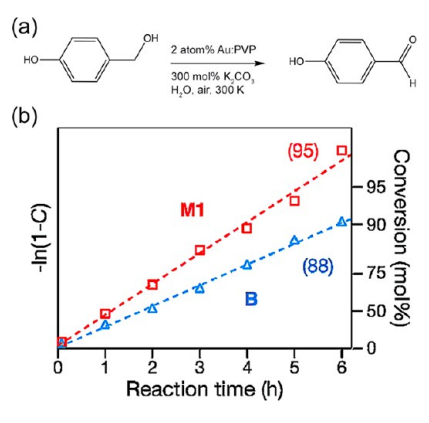


Figure 24. (a) Aerobic oxidation of *p*-hydroxylbenzyl alcohol to *p*-hydroxybenzaldehyde and (b) conversion to *p*-hydroxybenzaldehyde using the Au cluster catalyst made in flow (M1) and batch (B). The numbers in parentheses denote the product yield after 6 h. Reprinted with permission from ref 137. Copyright 2008 American Chemical Society.

Au coordination number and bond distance), as verified by X-ray absorption, that displays a higher inherent activity.

Bimetallic AuPd nanoclusters were also synthesized using a one-phase multilaminar flow mixing device for use as catalysts for the aerobic oxidation of benzyl alcohol. 140 The superior mixing due to the fast diffusion between laminar flows facilitates the synthesis of bimetallic structures with varying composition but in a smaller range of average crystallite sizes (1-3 nm). The origin of intrinsic synergistic effects resulting from the composition, not the size, could therefore be elucidated. The microfluidic multilamination mixer device consisted of 92 zirconia channels configured in an interdigitated pattern that were 15 μ m wide. Syringe pumps flowed the two aqueous solutions of (1) HAuCl₄, H₂PdCl₄, and PVP and (2) NaBH₄ and PVP into their respective inlets through 1 mm i.d. PTFE tubing (Figure 25a). The triangular focusing region allowed for mixing between the two solutions within 22 ms at a total flow rate of 32 mL min⁻¹. In order to achieve various compositions, the Au and Pd precursors were simply varied while maintaining a constant total metal precursor concentration of 10 mM. The throughput of the various stoichiometries was ~25-45 g per day, assuming complete metal precursor conversion. The compositions of the synthesized nanoparticles were nearly identical to the nominal amounts. Additionally, all compositions displayed a face centered cubic crystal structure as characterized by powder X-ray diffraction. Since the size and crystal structure are nearly identical for all compositions, the effect of varying composition ratios on their catalytic activity can be elucidated.

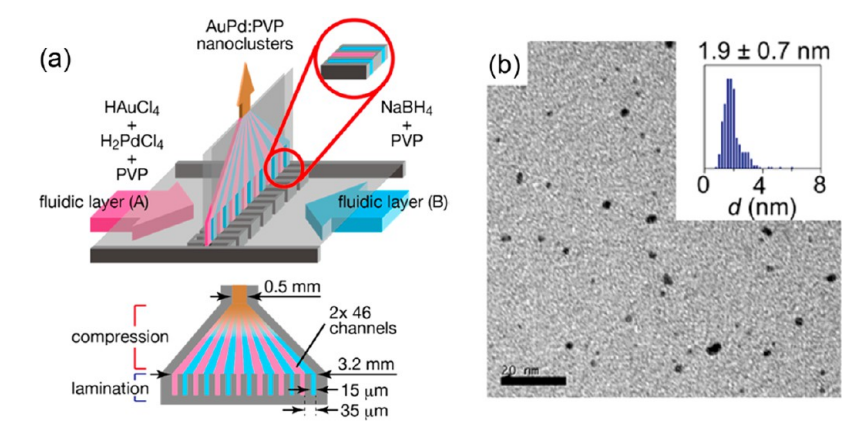


Figure 25. (a) Diagram of the one-phase laminar flow micromixer used for the fabrication of AuPd nanoparticles (top). Side cross-sectional view of the microlamination and compression zone for the 92 interdigitated channels (bottom). (b) TEM image and size distribution of Au₃Pd₅ nanoparticles fabricated in flow. Reprinted with permission from ref 140. Copyright 2014 American Chemical Society.

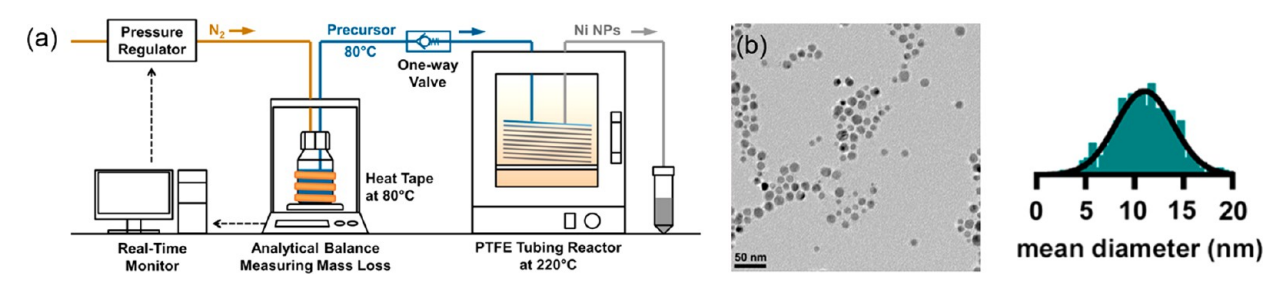


Figure 26. (a) Schematic of pressure-driven millifluidic reactor for the single-phase flow synthesis of Ni nanoparticles. (b) TEM image and size distribution of resulting Ni nanoparticles from the flow reactor. Reprinted with permission from ref 37. Copyright 2017 American Chemical Society.

The catalytic reaction was investigated using a setup identical to the aforementioned aerobic oxidation of phydroxylbenzyl alcohol reaction but using benzyl alcohol as the substrate. The major products for all bimetallic nanoparticles after 15 min were benzaldehyde and benzoic acid, with a minor product of benzylbenzoate, as determined by gas chromatography. Au and Pd nanoparticles were also investigated as a comparison, with Au displaying results similar to the bimetallic nanoparticles, but Pd displaying much less activity as indicated by the poor yield. The selectivity of the various compositions with respect to benzaldehyde was compared by normalizing the activity by the surface atoms as determined by the density of the bulk and the nanoparticle size. For $Au_{1-x}Pd_x$, where x = 0.20, the activity increases but then plateaus at x = 0.20-0.65, decreasing again with higher amounts of Pd, with the lowest activity being for pure Pd. Further characterization of the catalyst supported the hypothesis that the surface Au sites are the active sites, as confirmed by comparison of the high-resolution X-ray photoelectron spectroscopy regions of pure Au and Pd to Au₆Pd₄ and Au₈Pd₂ in which the Au 4f peaks shift to lower binding energies with increasing Pd content, strongly suggesting electron donation from Pd to Au in the bimetallic structures. Moreover, the Au₅Pd₅ nanoparticles made in flow exhibited both higher catalytic activity and selectivity to similarly sized Au₅Pd₅ nanoparticles made in batch for the oxidation of p-hydroxylbenzyl alcohol.

4.4. Nanofabrication of Hydrodeoxygenation Catalyst. The conversion of lignocellulosic biomass into useable liquid fuels that are compatible with current infrastructure requires the successful transformation of highly oxygenated

and high molecular weight biomass into high-value hydrocarbon products.¹⁴¹ The ex situ catalytic fast pyrolysis of lignocellulosic biomass is a process to upgrade pyrolysis vapors prior to condensation of a bio-oil; hydrodeoxygenation catalysts are needed to remove oxygen from the highly oxygenated feedstocks. Recently, it has been reported that various metal nanoparticle catalysts are competent for hydrodeoxygenation of biomass relevant substrates. 142-144 Recently, Brutchey and co-workers developed a one-phase millifluidic flow reactor to synthesize Ni nanoparticles as hydrodeoxygenation catalysts for the upgrading of biomass.³⁷ The reactor was constructed out of 200 ft of PTFE tubing (i.d. = 1.59 mm) that was heated using a convection oven (Figure 26a). The precursor solution of Ni(acac)₂, oleylamine, tri-noctylphosphine, and 1-octadecene was maintained at 80 °C. An analytical balance constantly monitored the flux of the precursor solution in real time, and a computer-controlled system adjusted the precursor solution driving pressure via a feedback loop to achieve a constant flow rate during the length of the run. The precursor solution flowed through a one-way check valve to mitigate against any potential back-flow resulting from the downstream gas evolution. Rapid nucleation was achieved upon the precursor solution entering the reactor (220 °C) as evident by the color change from green to black. Additionally, the elevated temperature caused massive gas evolution with a rate of 317 mL h⁻¹ that resulted in the stream being separated into discrete plugs, characteristic of two-phase flow, and resulted in a residence time of 16 min. The flowsynthesized Ni nanoparticles displayed an average diameter of 11.1 ± 3.1 nm (Figure 26b) with a yield of 62%, which equates to a throughput of >27 g of Ni nanoparticles per day on a

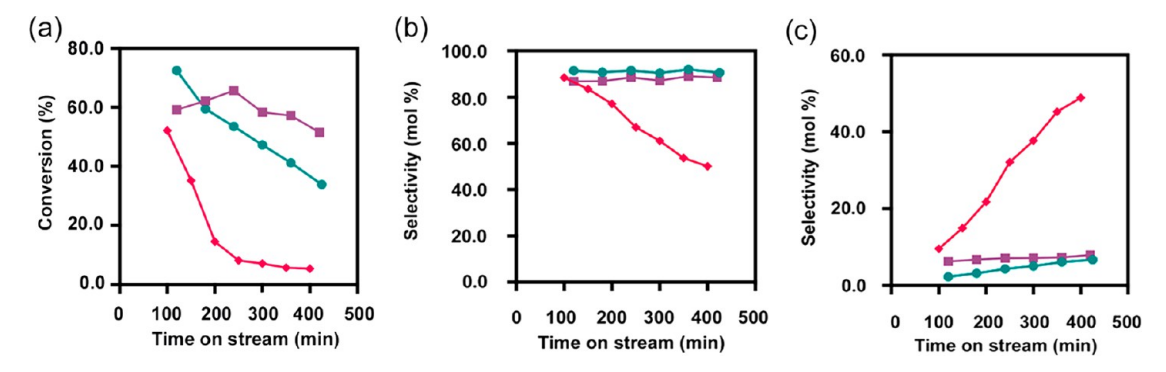


Figure 27. (a) Catalytic conversion of guaiacol as a function of time on stream. Hydrodeoxygenation selectivity in terms of (b) one- and (c) twooxygen-containing products under ex situ catalytic fast pyrolysis conditions for flow-synthesized Ni nanoparticles (green), batch-synthesized Ni nanoparticles (purple), and incipient wetness synthesized Ni nanoparticles (pink), all supported on silica. Reprinted with permission from ref 37. Copyright 2017 American Chemical Society.

single-channel device. Compared to an analogous batch reaction, the flow-synthesized Ni nanoparticles were smaller and synthesized in higher yields than the batch reaction producing Ni nanoparticles with an average size of 8.8 ± 2.4 nm and a 45% yield. The higher yield for the particles synthesized in flow is attributed to the superior heat and mass transport properties resulting from the millifluidic flow reactor.

Both the flow- and batch-synthesized Ni nanoparticles were supported on high-surface-area amorphous SiO₂ (5 wt %) to investigate their catalytic activity for the hydrodeoxygenation of guaiacol. An incipient wetness impregnation synthesized Ni/ SiO₂ catalyst was synthesized for comparison. This had larger, more polydisperse particles (15.4 \pm 7.4 nm) compared to the colloidal methods. Ex situ catalytic fast pyrolysis was performed by placing 0.35 g of catalyst mixed with silicon carbide into a tubular reactor at 350 $^{\circ}\text{C}$ and 0.5 MPa and fed with 5/95 argon/H₂ mixture (%) and guaiacol such that 12 mol of H2 was fed per mole of guaiacol. A weight hourly space velocity of 7 h⁻¹ was employed, which is the ratio of the mass flow rate of guaiacol to the catalyst mass. The effluent was characterized by gas chromatography at multiple intervals during time on stream.

The conversion of guaiacol to liquid products provided insight into the general activity of the three catalysts. The incipient wetness synthesized Ni/SiO₂ nanoparticles deactivated rapidly, whereas the continuous flow synthesized and batch-synthesized Ni/SiO₂ nanoparticles displayed minimal deactivation (Figure 27a). The conversion of the twooxygenated guaiacol model compound results in a wide array of products. Comparing the three catalysts for their selectivity toward one- and two-oxygen-containing products highlights the superior activity and stability of the colloidal nanoparticles compared to the incipient wetness catalyst. First, the selectivity of the flow- and batch-synthesized nanoparticles to oneoxygen-containing products is high with the main product being phenol (Figure 27b). However, with time on stream it is evident that the incipient wetness nanoparticles become less selective, which is compensated for by the increase in production of two-oxygen-containing products as seen in Figure 27b,c. Over time, the incipient wetness catalyst displays a higher selectivity toward the two-oxygen-containing catechol, which is a known catalyst poison (coke precursor and active site blocker) and supports the rapid deactivation in activity of the catalyst compared to the colloid Ni/SiO2 as seen in Figure 27a. 145-147 Overall, the colloidal catalysts behaved similarly, while the incipient wetness catalyst was more susceptible to

deactivation showing the viability of using continuous flow methods to synthesize colloidal Ni nanoparticles that behave comparably to the batch-synthesized catalyst.

5. CONCLUDING REMARKS AND FUTURE OUTLOOK

This Review delivers a compendium of recent literature regarding the continuous flow synthesis of various metal nanoparticle catalysts for hydrogenation, oxidation, and electrochemical reactions. While colloidal metal nanoparticle catalysts have yet to heavily infiltrate the commercial market due to the absence of large-scale synthetic procedures that provide high control over the resulting size, size distribution, and shape of the resulting material, the translation of nanoparticle batch syntheses to continuous flow methods affords a practical solution. The motivation for the implementation of colloidal nanoparticle catalysts is multifold: (1) the improved catalytic performance compared to their bulk counterparts, (2) the higher surface-area-to-volume ratio, (3) the enhanced control over surface-function properties, and (4) compositional tunability.

Continuous flow methods have afforded the ability to synthesize well-defined nanoparticles of a range of metals allowing for control over metal nanoparticle shape (Rh multipods¹¹³ and Pd icosahedra¹²⁵ and nanorods⁹⁵), size (Ag, ¹⁰⁸ Au, ¹³⁷ and Pd nanoparticles^{98,125}), and composition (PtNi, 97 PtBi, 81 and AuPd nanoparticles 82) for specific catalytic reactions. For the material systems that were compared to nanoparticles prepared via analogous batch reactions, the catalytic activity and/or selectivity was comparable, if not improved, for the nanoparticles produced in flow, which tend to be smaller and less polydisperse. 37,82,98,137,140 The ability to utilize a myriad of reactor designs to fabricate these nanoparticle catalysts under various conditions dictated by their reaction chemistry demonstrates the broad potential of continuous flow methods to synthesize material at scale.

While the vast majority of colloidal nanoparticle catalysts that have been fabricated in flow are metals or metal alloys, there are a few examples of oxides such as Fe₃O₄¹⁴⁸ and CeO₂¹⁴⁹ nanoparticles, as well as Ag/AgCl/ZnO¹⁵⁰ and FePt/ CeO_x nanoparticle hybrids, ¹⁵¹ that have been made in flow and shown to be competent catalysts. There is a growing body of work, however, on the continuous flow synthesis of colloidal metal oxide, ^{152–155} metal chalcogenide, ^{156–159} metal halide, ^{160,161} and metal pnictide nanoparticles. ^{162,163} This opens the possibility to use those flow-synthesized colloidal nanoparticles as catalysts and compare their catalytic performance to batch-synthesized equivalents, as has been done with the metal nanoparticles discussed here. As flow methods are extended to other material families of catalytically active nanoparticles, such as metal phosphides and metal carbides, the significantly higher temperatures needed for phosphidation and carburization will dictate reactor designs that tolerate higher temperature conditions.

With respect to the development of new colloidal nanoparticle catalysts, the parameter space for nanoparticle synthesis is high-dimensional and complicated, spanning a large number of variables such as temperature, residence time, precursor ratios, and concentrations. Optimization of the nanoparticle catalyst characteristics, such as size, size distribution, and morphology, is typically done one variable at a time in batch—this large parameter space makes optimization costly and time-consuming. 164 The highthroughput nature of continuous flow allows for much faster parametric screening for nanoparticle optimization. 165 By combining high-throughput continuous flow nanofabrication with in-line analytical tools, machine-learning algorithms can be used for automated optimization with respect to both product (nanoparticle attributes) and process (throughput, energy input, and so on). 166,167 In this way, the next generation of continuous flow reactors will sense and correct production irregularities to ensure nanoparticle catalyst fidelity, quality, and throughput at lower cost and reduced time. To date, the in-line analytical tools used for nanoparticle characterization in flow have been mainly limited to absorption and fluorescence spectroscopies, which can probe colloidal nanoparticles with spectroscopic signatures such as plasmon resonances or band edge emission. 168,169 More work needs to be done on developing additional in-line analytical tools to more generally monitor nanoparticle formation in continuous flow, such as small-angle X-ray scattering (SAXS). 170,171 Developing downstream methods of purifying and concentrating nanoparticle suspensions in flow will further complete process automation. 172

As continuous flow reactors are scaled out to a true advanced manufacturing technology through parallelization, life cycle analyses and techno-economic analyses need to be performed comparing the process to other methods currently being used to fabricate nanoparticle catalysts. Previous analysis of traditional syntheses of engineered nanoparticles suggest that any gains derived from the use of nanoparticles are currently offset by the methods used to manufacture them. 173 This presents an added challenge of scaling with flow reactors with an eye toward sustainability.

AUTHOR INFORMATION

Corresponding Authors

*(N.M.) E-mail: malmstad@usc.edu. *(R.L.B.) E-mail: brutchey@usc.edu.

Lu Wang: 0000-0002-4136-8261

Noah Malmstadt: 0000-0002-1786-2614 Richard L. Brutchey: 0000-0002-7781-5596

Notes

The authors declare no competing financial interest.

ACKNOWLEDGMENTS

R.L.B. and N.M. acknowledge NSF for supporting our nanomanufacturing work under CMMI-1728649.

REFERENCES

- (1) Synthesis of Solid Catalysts; de Jong, K. P., Ed.; Wiley-VCH Verlag: Weinheim, Germay, , 2009; DOI: 10.1002/9783527626854.
- (2) Schaidle, J. A.; Habas, S. E.; Baddour, F. G.; Farberow, C. A.; Ruddy, D. A.; Hensley, J. E.; Brutchey, R. L.; Malmstadt, N.; Robota, H. Transitioning Rationally Designed Catalytic Materials to Real "Working" Catalysts Produced at Commercial Scale: Nanoparticle Materials. In Catalysis; Spivey, J., Han, Y.-F., Eds.; Royal Society of Chemistry: Cambridge, U.K., 2017; Vol. 29, pp 213-281, DOI: 10.1039/9781788010634-00213.
- (3) Roduner, E. Size Matters: Why Nanomaterials Are Different. Chem. Soc. Rev. 2006, 35, 583-592.
- (4) Zhou, W. P.; Lewera, A.; Larsen, R.; Masel, R. I.; Bagus, P. S.; Wieckowski, A. Size Effects in Electronic and Catalytic Properties of Unsupported Palladium Nanoparticles in Electrooxidation of Formic Acid. J. Phys. Chem. B 2006, 110, 13393-13398.
- (5) Cuenya, B. R. Synthesis and Catalytic Properties of Metal Nanoparticles: Size, Shape, Support, Composition, and Oxidation State Effects. Thin Solid Films 2010, 518, 3127-3150.
- (6) Cortie, M. B. The Weird World of Nanoscale Gold. Gold Bull. **2004**, 37, 12-19.
- (7) El-Sayed, M. A. Small Is Different: Shape-, Size-, and Composition-Dependent Properties of Some Colloidal Semiconductor Nanocrystals. Acc. Chem. Res. 2004, 37, 326-333.
- (8) Schwarz, J. A.; Contescu, C.; Contescu, A. Methods for Preparation of Catalytic Materials. Chem. Rev. 1995, 95, 477-510.
- (9) Perego, C.; Villa, P. Catalyst Preparation Methods. Catal. Today 1997, 34, 281-305.
- (10) Scherzer, J.; Gruia, A. J. Hydrocracking Science and Technology; CRC Press: Boca Raton, FL, USA, 1996.
- (11) Preparation of Supported Catalysts. In Catalysis: An Integrated Approach to Homogeneous, Heterogeneous and Industrial Catalysis; Moulijn, J. A., van Leeuwen, P. W. N. M., van Santen, R. A., Eds.; Studies in Surface Science and Catalysis; Elsevier: Amsterdam, 1993; Vol. 79, Chapter 9, pp 335-360.
- (12) Thanh, N. T. K.; Maclean, N.; Mahiddine, S. Mechanisms of Nucleation and Growth of Nanoparticles in Solution. Chem. Rev. **2014**, 114, 7610-7630.
- (13) Lee, J.; Yang, J.; Kwon, S. G.; Hyeon, T. Nonclassical Nucleation and Growth of Inorganic Nanoparticles. Nat. Rev. Mater. 2016, 1, 16034-16050.
- (14) Wu, Z.; Yang, S.; Wu, W. Shape Control of Inorganic Nanoparticles from Solution. Nanoscale 2016, 8, 1237-1259.
- (15) Yin, Y.; Alivisatos, A. P. Colloidal Nanocrystal Synthesis and the Organic-Inorganic Interface. Nature 2005, 437, 664-670.
- (16) Kumar, S.; Nann, T. Shape Control of II-VI Semiconductor Nanomaterials. Small 2006, 2, 316-329.
- (17) Heuer-Jungemann, A.; Feliu, N.; Bakaimi, I.; Hamaly, M.; Alkilany, A.; Chakraborty, I.; Masood, A.; Casula, M. F.; Kostopoulou, A.; Oh, E.; Susumu, K.; Stewart, M. H.; Medintz, I. L.; Stratakis, E.; Parak, W. J.; Kanaras, A. G. The Role of Ligands in the Chemical Synthesis and Applications of Inorganic Nanoparticles. Chem. Rev. 2019, 119, 4819-4880.
- (18) Wu, J.; Gross, A.; Yang, H. Shape and Composition-Controlled Platinum Alloy Nanocrystals Using Carbon Monoxide as Reducing Agent. Nano Lett. 2011, 11, 798-802.
- (19) Ahrenstorf, K.; Albrecht, O.; Heller, H.; Kornowski, A.; Görlitz, D.; Weller, H. Colloidal Synthesis of Ni_xPt_{1-x} Nanoparticles with Tuneable Composition and Size. Small 2007, 3, 271-274.
- (20) Park, J. Y.; Zhang, Y.; Grass, M.; Zhang, T.; Somorjai, G. A. Tuning of Catalytic CO Oxidation by Changing Composition of Rh-Pt Bimetallic Nanoparticles. Nano Lett. 2008, 8, 673-677.
- (21) Xu, D.; Bliznakov, S.; Liu, Z.; Fang, J.; Dimitrov, N. Composition-Dependent Electrocatalytic Activity of Pt-Cu Nanocube

- Catalysts for Formic Acid Oxidation. Angew. Chem., Int. Ed. 2010, 49, 1282-1285.
- (22) Guo, S.; Zhang, S.; Sun, S. Tuning Nanoparticle Catalysis for the Oxygen Reduction Reaction. Angew. Chem., Int. Ed. 2013, 52, 8526-8544.
- (23) Yuan, Y.; Yan, N.; Dyson, P. J. Advances in the Rational Design of Rhodium Nanoparticle Catalysts: Control via Manipulation of the Nanoparticle Core and Stabilizer. ACS Catal. 2012, 2, 1057-1069.
- (24) Hunt, S. T.; Román-Leshkov, Y. Principles and Methods for the Rational Design of Core-Shell Nanoparticle Catalysts with Ultralow Noble Metal Loadings. Acc. Chem. Res. 2018, 51, 1054-1062.
- (25) Huang, W.; Li, W.-X. Surface and Interface Design for Heterogeneous Catalysis. Phys. Chem. Chem. Phys. 2019, 21, 523-536.
- (26) Bratlie, K. M.; Lee, H.; Komvopoulos, K.; Yang, P.; Somorjai, G. A. Platinum Nanoparticle Shape Effects on Benzene Hydrogenation Selectivity. Nano Lett. 2007, 7, 3097-3101.
- (27) Crespo-Quesada, M.; Yarulin, A.; Jin, M.; Xia, Y.; Kiwi-Minsker, L. Structure Sensitivity of Alkynol Hydrogenation on Shapeand Size-Controlled Palladium Nanocrystals: Which Sites Are Most Active and Selective? J. Am. Chem. Soc. 2011, 133, 12787-12794.
- (28) Narayanan, R.; El-Sayed, M. A. Shape-Dependent Catalytic Activity of Platinum Nanoparticles in Colloidal Solution. Nano Lett. 2004, 4, 1343-1348.
- (29) Shao, M.; Peles, A.; Shoemaker, K. Electrocatalysis on Platinum Nanoparticles: Particle Size Effect on Oxygen Reduction Reaction Activity. Nano Lett. 2011, 11, 3714-3719.
- (30) Liu, G.; Yu, J. C.; Lu, G. Q. M.; Cheng, H.-M. Crystal Facet Engineering of Semiconductor Photocatalysts: Motivations, Advances and Unique Properties. Chem. Commun. 2011, 47, 6763-6783.
- (31) Narayanan, R.; El-Sayed, M. A. Catalysis with Transition Metal Nanoparticles in Colloidal Solution: Nanoparticle Shape Dependence and Stability. J. Phys. Chem. B 2005, 109, 12663-12676.
- (32) Xu, R.; Wang, D.; Zhang, J.; Li, Y. Shape-Dependent Catalytic Activity of Silver Nanoparticles for the Oxidation of Styrene. Chem. -Asian J. 2006, 1, 888-893.
- (33) Advances in Transport Phenomena; Wang, L., Ed.; Springer: Heidelberg, Germany, 2010; DOI: 10.1007/978-3-642-19466-5.
- (34) Hartman, R. L.; McMullen, J. P.; Jensen, K. F. Deciding Whether To Go with the Flow: Evaluating the Merits of Flow Reactors for Synthesis. Angew. Chem., Int. Ed. 2011, 50, 7502-7519.
- (35) Epps, R. W.; Felton, K. C.; Coley, C. W.; Abolhasani, M. Automated Microfluidic Platform for Systematic Studies of Colloidal Perovskite Nanocrystals: Towards Continuous Nanomanufacturing. Lab Chip 2017, 17, 4040-4047.
- (36) Riche, C. T.; Roberts, E. J.; Gupta, M.; Brutchey, R. L.; Malmstadt, N. Flow Invariant Droplet Formation for Stable Parallel Microreactors. Nat. Commun. 2016, 7, 10780.
- (37) Roberts, E. J.; Habas, S. E.; Wang, L.; Ruddy, D. A.; White, E. A.; Baddour, F. G.; Griffin, M. B.; Schaidle, J. A.; Malmstadt, N.; Brutchey, R. L. High-Throughput Continuous Flow Synthesis of Nickel Nanoparticles for the Catalytic Hydrodeoxygenation of Guaiacol. ACS Sustainable Chem. Eng. 2017, 5, 632-639.
- (38) Ahrberg, C. D.; Choi, J. W.; Chung, B. G. Droplet-Based Synthesis of Homogeneous Magnetic Iron Oxide Nanoparticles. Beilstein J. Nanotechnol. 2018, 9, 2413-2420.
- (39) Cottam, B. F.; Krishnadasan, S.; deMello, A. J.; deMello, J. C.; Shaffer, M. S. P. Accelerated Synthesis of Titanium Oxide Nanostructures Using Microfluidic Chips. Lab Chip 2007, 7, 167-
- (40) Lab on a Chip Technology: Fabrication and Microfluidics, Vol. 1; Herold, K. E., Rasooly, A., Eds.; Caister Academic Press: Haverhill, U.K., 2009.
- (41) Topics in current chemistry: Microfluidics: Technologies and Applications; Lin, B., Basuray, S., Eds.; Springer: Heidelberg, 2011; DOI: 10.1007/978-3-642-27004-8.
- (42) Hessel, V.; Löwe, H.; Schönfeld, F. Micromixers—A Review on Passive and Active Mixing Principles. Chem. Eng. Sci. 2005, 60, 2479-2501.

- (43) Ward, K.; Fan, Z. H. Mixing in Microfluidic Devices and Enhancement Methods. J. Micromech. Microeng. 2015, 25, 094001-
- (44) Microfluidic Devices in Nanotechnology: Fundamental Concepts; Kumar, C., Ed.; John Wiley & Sons: Hoboken, NJ, USA, 2010; DOI: 10.1002/9780470622636.
- (45) Springer Handbook of Experimental Fluid Mechanics; Tropea, C., Yarin, A. L., Foss, J. F., Eds.; Springer: Heidelberg, Germany, 2007.
- (46) Kamholz, A. E.; Yager, P. Theoretical Analysis of Molecular Diffusion in Pressure-Driven Laminar Flow in Microfluidic Channels. Biophys. J. 2001, 80, 155-160.
- (47) Angelescu, D. E. Highly Integrated Microfluidics Design; Artech House: Boston, MA, USA, 2011.
- (48) Hessel, V.; Hardt, S.; Löwe, H.; Schönfeld, F. Laminar Mixing in Different Interdigital Micromixers: I. Experimental Characterization. AIChE J. 2003, 49, 566-577.
- (49) Sudarsan, A. P.; Ugaz, V. M. Multivortex Micromixing. Proc. Natl. Acad. Sci. U. S. A. 2006, 103, 7228-7233.
- (50) Carrier, O.; Funfschilling, D.; Debas, H.; Poncin, S.; Löb, P.; Li, H.-Z. Pressure Drop in a Split-and-Recombine Caterpillar Micromixer in Case of Newtonian and Non-Newtonian Fluids. AIChE J. 2013, 59, 2679-2685.
- (51) Microfluidic Methods for Molecular Biology; Lu, C., Verbridge, S. S., Eds.; Springer International: Cham, Switzerland, 2016; DOI: 10.1007/978-3-319-30019-1.
- (52) Schönfeld, F.; Hardt, S. Simulation of Helical Flows in Microchannels. AIChE J. 2004, 50, 771-778.
- (53) Song, H.; Chen, D. L.; Ismagilov, R. F. Reactions in Droplets in Microfluidic Channels. Angew. Chem., Int. Ed. 2006, 45, 7336-7356.
- (54) Günther, A.; Jensen, K. F. Multiphase Microfluidics: From Flow Characteristics to Chemical and Materials Synthesis. Lab Chip 2006, 6, 1487-1503.
- (55) Nightingale, A. M.; deMello, J. C. Segmented Flow Reactors for Nanocrystal Synthesis. Adv. Mater. 2013, 25, 1813-1821.
- (56) Ottino, J. M. The Kinematics of Mixing: Stretching, Chaos, and Transport; Cambridge University Press: Cambridge, U.K., 1989.
- (57) Bringer, M. R.; Gerdts, C. J.; Song, H.; Tice, J. D.; Ismagilov, R. F. Microfluidic Systems for Chemical Kinetics That Rely on Chaotic Mixing in Droplets. Philos. Transact. A Math. Phys. Eng. Sci. 2004, 362, 1087-1104.
- (58) Baroud, C. N.; Gallaire, F.; Dangla, R. Dynamics of Microfluidic Droplets. Lab Chip 2010, 10, 2032-2045.
- (59) Anna, S. L.; Bontoux, N.; Stone, H. A. Formation of Dispersions Using "Flow Focusing" in Microchannels. Appl. Phys. Lett. 2003, 82, 364-366.
- (60) Wehking, J. D.; Gabany, M.; Chew, L.; Kumar, R. Effects of Viscosity, Interfacial Tension, and Flow Geometry on Droplet Formation in a Microfluidic T-Junction. Microfluid. Nanofluid. 2014, 16, 441-453.
- (61) Lazarus, L. L.; Riche, C. T.; Marin, B. C.; Gupta, M.; Malmstadt, N.; Brutchey, R. L. Two-Phase Microfluidic Droplet Flows of Ionic Liquids for the Synthesis of Gold and Silver Nanoparticles. ACS Appl. Mater. Interfaces 2012, 4, 3077-3083.
- (62) Liu, H.; Zhang, Y. Droplet Formation in a T-Shaped Microfluidic Junction. J. Appl. Phys. 2009, 106, 034906-034914.
- (63) Microfluidics for Pharmaceutical Applications: From Nano/Micro Systems Fabrication to Controlled Drug Delivery; Santos, H. A., Liu, D., Zhang, H., Eds.; Elsevier: Amsterdam, The Netherlands, 2018; DOI: 10.1016/C2016-0-03449-6.
- (64) Abate, A. R.; Lee, D.; Do, T.; Holtze, C.; Weitz, D. A. Glass Coating for PDMS Microfluidic Channels by Sol-Gel Methods. Lab Chip 2008, 8, 516-518.
- (65) Ohtani, K.; Tsuchiya, M.; Sugiyama, H.; Katakura, T.; Hayakawa, M.; Kanai, T. Surface Treatment of Flow Channels in Microfluidic Devices Fabricated by Stereolithography. J. Oleo Sci. 2014, 63, 93-96.
- (66) Tropmann, A.; Tanguy, L.; Koltay, P.; Zengerle, R.; Riegger, L. Completely Superhydrophobic PDMS Surfaces for Microfluidics. Langmuir 2012, 28, 8292-8295.

- (67) Zhou, J.; Ellis, A. V.; Voelcker, N. H. Recent Developments in PDMS Surface Modification for Microfluidic Devices. Electrophoresis 2010, 31, 2-16.
- (68) Xu, J. H.; Li, S. W.; Tan, J.; Wang, Y. J.; Luo, G. S. Preparation of Highly Monodisperse Droplet in a T-junction Microfluidic Device. AIChE J. 2006, 52, 3005-3010.
- (69) Costa, A. L. R.; Gomes, A.; Cunha, R. L. Studies of Droplets Formation Regime and Actual Flow Rate of Liquid-Liquid Flows in Flow-Focusing Microfluidic Devices. Exp. Therm. Fluid Sci. 2017, 85,
- (70) Anna, S. L.; Bontoux, N.; Stone, H. A. Formation of Dispersions Using "Flow Focusing" in Microchannels. Appl. Phys. Lett. 2003, 82, 364-366.
- (71) Tan, Y.-C.; Cristini, V.; Lee, A. P. Monodispersed Microfluidic Droplet Generation by Shear Focusing Microfluidic Device. Sens. Actuators, B 2006, 114, 350-356.
- (72) Gupta, A.; Murshed, S. M. S.; Kumar, R. Droplet Formation and Stability of Flows in a Microfluidic T-Junction. Appl. Phys. Lett. 2009, 94, 164107-164110.
- (73) Krishnadasan, S.; Brown, R. J. C.; deMello, A. J.; deMello, J. C. Intelligent Routes to the Controlled Synthesis of Nanoparticles. Lab Chip 2007, 7, 1434-1441.
- (74) Jiao, Z.; Zhao, J.; Chao, Z.; You, Z.; Zhao, J. An Air-Chamber-Based Microfluidic Stabilizer for Attenuating Syringe-Pump-Induced Fluctuations. Microfluid. Nanofluid. 2019, 23, 26.
- (75) Unger, M. A.; Chou, H.-P.; Thorsen, T.; Scherer, A.; Quake, S. R. Monolithic Microfabricated Valves and Pumps by Multilayer Soft Lithography. Science 2000, 288, 113-116.
- (76) Yang, S.-Y.; Cheng, F.-Y.; Yeh, C.-S.; Lee, G.-B. Size-Controlled Synthesis of Gold Nanoparticles Using a Micro-Mixing System. Microfluid. Nanofluid. 2010, 8, 303-311.
- (77) Tecnoflon FKM & PFR FFKM. Solvay, https://www.solvay. com/en/products/brands/tecnoflon-fkm-pfr-ffkm.
- (78) The Most Durable and Dependable Fluoroelastomer Tubing. W. L. Gore Associates, Elkton, MD, USA, http://www.hollandapt. com/Documents/Ctrl Hyperlink/Gore Chem-Sure Tube 400 uid172010859361.pdf (accessed Apr .14, 2019).
- (79) Fkm Rubber Compounding. Polycomp, Vorden, The Netherlands, https://www.polycomp.nl/fkm-advantages/ (accessed Feb. 28,
- (80) Dong, M. W. Modern HPLC for Practicing Scientists; John Wiley & Sons: Hoboken, NJ, USA, 2006; DOI: 10.1002/0471973106.
- (81) Zhang, D.; Wu, F.; Peng, M.; Wang, X.; Xia, D.; Guo, G. One-Step, Facile and Ultrafast Synthesis of Phase-and Size-Controlled Pt-Bi Intermetallic Nanocatalysts through Continuous-Flow Microfluidics. J. Am. Chem. Soc. 2015, 137, 6263-6269.
- (82) Tofighi, G.; Gaur, A.; Doronkin, D. E.; Lichtenberg, H.; Wang, W.; Wang, D.; Rinke, G.; Ewinger, A.; Dittmeyer, R.; Grunwaldt, J.-D. Microfluidic Synthesis of Ultrasmall AuPd Nanoparticles with a Homogeneously Mixed Alloy Structure in Fast Continuous Flow for Catalytic Applications. J. Phys. Chem. C 2018, 122, 1721-1731.
- (83) Tofighi, G.; Lichtenberg, H.; Pesek, J.; Sheppard, T. L.; Wang, W.; Schottner, L.; Rinke, G.; Dittmeyer, R.; Grunwaldt, J.-D. Continuous Microfluidic Synthesis of Colloidal Ultrasmall Gold Nanoparticles: In situ Study of the Early Reaction Stages and Application for Catalysis. React. Chem. Eng. 2017, 2, 876-884.
- (84) Zeng, W.; Li, S.; Wang, Z. Characterization of Syringe-Pump-Driven versus Pressure-Driven Microfluidic Flows. In 2015 International Conference on Fluid Power and Mechatronics (FPM) 2015, 711-
- (85) Begolo, S.; Zhukov, D. V.; Selck, D. A.; Li, L.; Ismagilov, R. F. The Pumping Lid: Investigating Multi-Material 3D Printing for Equipment-Free, Programmable Generation of Positive and Negative Pressures for Microfluidic Applications. Lab Chip 2014, 14, 4616-
- (86) Mukhopadhyay, R. When Microfluidic Devices Go Bad. Anal. Chem. 2005, 77, 429A-432A.

- (87) Schoenitz, M.; Grundemann, L.; Augustin, W.; Scholl, S. Fouling in Microstructured Devices: A Review. Chem. Commun. 2015, 51, 8213-8228.
- (88) Wille, C.; Gabski, H.-P.; Haller, T.; Kim, H.; Unverdorben, L.; Winter, R. Synthesis of Pigments in a Three-Stage Microreactor Pilot Plant-An Experimental Technical Report. Chem. Eng. J. 2004, 101,
- (89) Rhee, M.; Valencia, P. M.; Rodriguez, M. I.; Langer, R.; Farokhzad, O. C.; Karnik, R. Synthesis of Size-Tunable Polymeric Nanoparticles Enabled by 3D Hydrodynamic Flow Focusing into Single-Layer Microchannels. Adv. Mater. 2011, 23, H79-H83.
- (90) Lameiras, F. S.; de Souza, A. L.; de Melo, V. A. R.; Nunes, E. H. M.; Braga, I. D. Measurement of the Zeta Potential of Planar Surfaces with a Rotating Disk. Mater. Res. 2008, 11, 217-219.
- (91) Bandulasena, M. V.; Vladisavljevic, G. T.; Odunmbaku, O. G.; Benyahia, B. Continuous Synthesis of PVP Stabilized Biocompatible Gold Nanoparticles with a Controlled Size Using a 3D Glass Capillary Microfluidic Device. Chem. Eng. Sci. 2017, 171, 233-243.
- (92) Li-Ching, T.; Xiao-Ping, S.; Yi-Yun, X.; Zheng-Liang, Z. Segmental Flow-Injection Analysis: Device and Applications. Anal. Chim. Acta 1990, 238, 183-190.
- (93) Cheng, D.; Jiang, H. A Debubbler for Microfluidics Utilizing Air-Liquid Interfaces. Appl. Phys. Lett. 2009, 95, 214103.
- (94) Van Lintel, H.; Mernier, G.; Renaud, P. High-Throughput Micro-Debubblers for Bubble Removal with Sub-Microliter Dead Volume. Micromachines 2012, 3, 218-224.
- (95) Sebastian, V.; Basak, S.; Jensen, K. F. Continuous Synthesis of Palladium Nanorods in Oxidative Segmented Flow. AIChE J. 2016, *62*, 373–380.
- (96) Zeng, C.; Wang, C.; Wang, F.; Zhang, Y.; Zhang, L. A Novel Vapor-Liquid Segmented Flow Based on Solvent Partial Vaporization in Microstructured Reactor for Continuous Synthesis of Nickel Nanoparticles. Chem. Eng. J. 2012, 204-206, 48-53.
- (97) Niu, G.; Zhou, M.; Yang, X.; Park, J.; Lu, N.; Wang, J.; Kim, M. J.; Wang, L.; Xia, Y. Synthesis of Pt-Ni Octahedra in Continuous-Flow Droplet Reactors for the Scalable Production of Highly Active Catalysts toward Oxygen Reduction. Nano Lett. 2016, 16, 3850-
- (98) Wong, W. K.; Yap, W. K.; Lim, Y. C.; Khan, S. A.; Pelletier, F.; Corbos, C. C. Robust, Non-Fouling Liters-per-Day Flow Synthesis of Ultra-Small Catalytically Active Metal Nanoparticles in a Single-Channel Reactor. React. Chem. Eng. 2017, 2, 636-641.
- (99) Conchouso, D.; Castro, D.; Khan, S. A.; Foulds, I. G. Three-Dimensional Parallelization of Microfluidic Droplet Generators for a Litre per Hour Volume Production of Single Emulsions. Lab Chip 2014, 14, 3011-3020.
- (100) Catalysis and Catalytic Processes. In Industrial Catalytic Processes for Fine and Specialty Chemicals; Ranade, V. V., Joshi, S. S., Eds.; Elsevier: Amsterdam, 2016; pp 1-14, DOI: 10.1016/B978-0-12-801457-8.00001-X.
- (101) Hydrogenation with Low-Cost Transition Metals; Sa, J., Srebowata, A., Eds.; Chapman and Hall/CRC Press: Boca Raton, FL, USA, 2015.
- (102) Lamture, J. B. Aniline and Its Analogs; Notion Press: Chennai, India, 2018.
- (103) Catalysis of Organic Reactions; Ford, M. E., Ed.; CRC Press: Boca Raton, FL, USA, 2000.
- (104) Industrial Organic Chemistry, 5th ed.; Arpe, H.-J., Ed.; Wiley-VCH: Weinheim, Germany, 2010.
- (105) Lloyd, L. Handbook of Industrial Catalysts; Springer Science & Business Media: Berlin, 2011; DOI: 10.1007/978-0-387-49962-8.
- (106) Muroi, T. Role of Precious Metal Catalysts. In Noble Metals; Su, Y.-H., Ed.; InTech: London, 2012; DOI: 10.5772/1916.
- (107) Unnikrishnan, P.; Srinivas, D. Heterogeneous Catalysis. In Industrial Catalytic Processes for Fine and Specialty Chemicals; Joshi, S. S., Ranade, V. V., Eds.; Elsevier: Amsterdam, 2016.
- (108) Wu, K.-J.; Torrente-Murciano, L. Continuous Synthesis of Tuneable Sized Silver Nanoparticles via a Tandem Seed-Mediated

- Method in Coiled Flow Inverter Reactors. React. Chem. Eng. 2018, 3, 267–276.
- (109) Wu, K.-J.; De Varine Bohan, G. M.; Torrente-Murciano, L. Synthesis of Narrow Sized Silver Nanoparticles in the Absence of Capping Ligands in Helical Microreactors. *React. Chem. Eng.* **2017**, *2*, 116–128
- (110) Hessel, V.; Hardt, S.; Löwe, H. Chemical Micro Process Engineering: Fundamentals, Modelling and Reactions; John Wiley & Sons: Weinheim, Germany, 2004.
- (111) Acres, G. J. K.; Swars, K. Pt Platinum: Supplement Vol. A 1 Technology of Platinum-Group Metals; Springer Science & Business Media: Berlin, 1985.
- (112) Jackson, S. D., Ed. Hydrogenation: Catalysts and Processes; Walter de Gruyter: Berlin, 2018.
- (113) Kunal, P.; Roberts, E. J.; Riche, C. T.; Jarvis, K.; Malmstadt, N.; Brutchey, R. L.; Humphrey, S. M. Continuous Flow Synthesis of Rh and RhAg Alloy Nanoparticle Catalysts Enables Scalable Production and Improved Morphological Control. *Chem. Mater.* **2017**, *29*, 4341–4350.
- (114) Xiong, Y.; Xia, Y. Shape-Controlled Synthesis of Metal Nanostructures: The Case of Palladium. *Adv. Mater.* **2007**, *19*, 3385–3391.
- (115) Xiong, Y.; Cai, H.; Wiley, B. J.; Wang, J.; Kim, M. J.; Xia, Y. Synthesis and Mechanistic Study of Palladium Nanobars and Nanorods. J. Am. Chem. Soc. 2007, 129, 3665–3675.
- (116) Electrocatalysts for Low Temperature Fuel Cells; Maiyalagan, T., Saji, V. S., Eds.; Wiley-VCH: Weinheim, Germany, 2017; DOI: 10.1002/9783527803873.
- (117) Yuan, X.-Z.; Wang, H. PEM Fuel Cell Fundamentals. In *PEM Fuel Cell Electrocatalysts and Catalyst Layers: Fundamentals and Applications*; Zhang, J., Ed.; Springer: London, 2008; pp 1–87, DOI: 10.1007/978-1-84800-936-3 1.
- (118) Zhang, J.; Yang, H.; Fang, J.; Zou, S. Synthesis and Oxygen Reduction Activity of Shape-Controlled Pt₃Ni Nanopolyhedra. *Nano Lett.* **2010**, *10*, 638–644.
- (119) Carpenter, M. K.; Moylan, T. E.; Kukreja, R. S.; Atwan, M. H.; Tessema, M. M. Solvothermal Synthesis of Platinum Alloy Nanoparticles for Oxygen Reduction Electrocatalysis. *J. Am. Chem. Soc.* **2012**, *134*, 8535–8542.
- (120) Sasaki, K.; Wang, J. X.; Naohara, H.; Marinkovic, N.; More, K.; Inada, H.; Adzic, R. R. Recent Advances in Platinum Monolayer Electrocatalysts for Oxygen Reduction Reaction: Scale-up Synthesis, Structure and Activity of Pt Shell on Pd Cores. *Electrochim. Acta* 2010, 55, 2645–2652.
- (121) Li, J.; Xi, Z.; Pan, Y.-T.; Spendelow, J. S.; Duchesne, P. N.; Su, D.; Li, Q.; Yu, C.; Yin, Z.; Shen, B.; Kim, Y. S.; Zhang, P.; Sun, S. Fe Stabilization by Intermetallic L1₀-FePt and Pt Catalysis Enhancement in L1₀-FePt/Pt Nanoparticles for Efficient Oxygen Reduction Reaction in Fuel Cells. *J. Am. Chem. Soc.* **2018**, *140*, 2926–2932.
- (122) Proton Conducting Membrane Fuel Cells IV: Proceedings of the International Symposium; Murthy, M., Ota, K., Van Zee, J. W., Narayanan, S. R., Takeuchi, E. S., Eds.; The Electrochemical Society: Pennington, NJ, USA, 2006.
- (123) Handbook of Fuel Cells: Advances in Electrocatalysis, Materials, Diagnostics and Durability; Vielstich, W.; Gasteiger, H. A.; Yokokawa, H., Eds.; John Wiley & Sons: Chichester, U.K., 2009.
- (124) Zhang, J.; Fang, J. A. General Strategy for Preparation of Pt 3d-Transition Metal (Co, Fe, Ni) Nanocubes. *J. Am. Chem. Soc.* **2009**, 131, 18543–18547.
- (125) Wang, H.; Niu, G.; Zhou, M.; Wang, X.; Park, J.; Bao, S.; Chi, M.; Cai, Z.; Xia, Y. Scalable Synthesis of Palladium Icosahedra in Plug Reactors for the Production of Oxygen Reduction Reaction Catalysts. *ChemCatChem* **2016**, *8*, 1658–1664.
- (126) Skrabalak, S. E.; Wiley, B. J.; Kim, M.; Formo, E. V.; Xia, Y. On the Polyol Synthesis of Silver Nanostructures: Glycolaldehyde as a Reducing Agent. *Nano Lett.* **2008**, *8*, 2077–2081.
- (127) Zhang, L.; Wang, Y.; Tong, L.; Xia, Y. Seed-Mediated Synthesis of Silver Nanocrystals with Controlled Sizes and Shapes in

- Droplet Microreactors Separated by Air. *Langmuir* **2013**, *29*, 15719–15725.
- (128) Wiley, W.; Herricks, T.; Sun, Y.; Xia, Y. Polyol Synthesis of Silver Nanoparticles: Use of Chloride and Oxygen to Promote the Formation of Single-Crystal, Truncated Cubes and Tetrahedrons. *Nano Lett.* **2004**, *4*, 1733–1739.
- (129) Zhang, L.; Roling, L. T.; Wang, X.; Vara, M.; Chi, M.; Liu, J.; Choi, S.; Park, J.; Herron, J. A.; Xie, Z.; Mavrikakis, M.; Xia, Y. Platinum-Based Nanocages with Subnanometer-Thick Walls and Well-Defined, Controllable Facets. *Science* **2015**, 349, 412–416.
- (130) Wang, X.; Choi, S.; Roling, L. T.; Luo, M.; Ma, C.; Zhang, L.; Chi, M.; Liu, J.; Xie, Z.; Herron, J. A.; Mavrikakis, M.; Xia, Y. Palladium-Platinum Core-Shell Icosahedra with Substantially Enhanced Activity and Durability Towards Oxygen Reduction. *Nat. Commun.* 2015, 6, 7594.
- (131) Ji, X.; Lee, K. T.; Holden, R.; Zhang, L.; Zhang, J.; Botton, G. A.; Couillard, M.; Nazar, L. F. Nanocrystalline Intermetallics on Mesoporous Carbon for Direct Formic Acid Fuel Cell Anodes. *Nat. Chem.* **2010**, *2*, 286–293.
- (132) Huang, S.; Hara, K.; Fukuoka, A. Green Catalysis for Selective CO Oxidation in Hydrogen for Fuel Cell. *Energy Environ. Sci.* **2009**, *2*, 1060–1068.
- (133) Lee, B. H. Fundamentals of Food Biotechnology; John Wiley & Sons, 2014; DOI: 10.1002/9781118384947.
- (134) The Chemistry of Fragrances: From Perfumer to Consumer; Sell, C. S., Ed.; Royal Society of Chemistry: Cambridge, U.K., 2006.
- (135) Mukhopadhyay, A. K. Industrial Chemical Cresols and Downstream Derivatives; CRC Press: Boca Raton, FL, USA, 2004.
- (136) Brühne, F.; Wright, E. Benzaldehyde. In *Ullmann's Encyclopedia of Industrial Chemistry*; Wiley-VCH Verlag: Weinheim, Germany, 2011.
- (137) Tsunoyama, H.; Ichikuni, N.; Tsukuda, T. Microfluidic Synthesis and Catalytic Application of PVP-Stabilized, ~ 1 Nm Gold Clusters. *Langmuir* **2008**, *24*, 11327–11330.
- (138) Hastelloy C-276 Nickel Alloy, UNS No. 10276, Alloy C276, Hastelloy C, Inconel C-276; MEGA MEX, Humble, TX, USA, http://megamex.com/hastelloy-c-276-c276-nickel-alloy.htm (accessed Mar. 25, 2019).
- (139) Tsunoyama, H.; Sakurai, H.; Ichikuni, N.; Negishi, Y.; Tsukuda, T. Colloidal Gold Nanoparticles as Catalyst for Carbon-Carbon Bond Formation: Application to Aerobic Homocoupling of Phenylboronic Acid in Water. *Langmuir* 2004, 20, 11293–11296.
- (140) Hayashi, N.; Sakai, Y.; Tsunoyama, H.; Nakajima, A. Development of Ultrafine Multichannel Microfluidic Mixer for Synthesis of Bimetallic Nanoclusters: Catalytic Application of Highly Monodisperse AuPd Nanoclusters Stabilized by Poly(*N*-Vinylpyrrolidone). *Langmuir* **2014**, *30*, 10539–10547.
- (141) Iliopoulou, E. F.; Stefanidis, S. D.; Kalogiannis, K. G.; Delimitis, A.; Lappas, A. A.; Triantafyllidis, K. S. Catalytic Upgrading of Biomass Pyrolysis Vapors Using Transition Metal-Modified ZSM-5 Zeolite. *Appl. Catal., B* **2012**, *127*, 281–290.
- (142) Luo, Z.; Zheng, Z.; Li, L.; Cui, Y.-T.; Zhao, C. Bimetallic Ru-Ni Catalyzed Aqueous-Phase Guaiacol Hydrogenolysis at Low H₂ Pressures. *ACS Catal.* **2017**, *7*, 8304–8313.
- (143) Offner-Marko, L.; Bordet, A.; Moos, G.; Tricard, S.; Rengshausen, S.; Chaudret, B.; Luska, K. L.; Leitner, W. Bimetallic Nanoparticles in Supported Ionic Liquid Phases as Multifunctional Catalysts for the Selective Hydrodeoxygenation of Aromatic Substrates. *Angew. Chem., Int. Ed.* **2018**, *57*, 12721–12726.
- (144) Fan, R.; Chen, C.; Han, M.; Gong, W.; Zhang, H.; Zhang, Y.; Zhao, H.; Wang, G. Highly Dispersed Copper Nanoparticles Supported on Activated Carbon as an Efficient Catalyst for Selective Reduction of Vanillin. *Small* **2018**, *14*, 1801953.
- (145) Foo, G. S.; Rogers, A. K.; Yung, M. M.; Sievers, C. Steric Effect and Evolution of Surface Species in the Hydrodeoxygenation of Bio-Oil Model Compounds over Pt/HBEA. *ACS Catal.* **2016**, *6*, 1292–1307.
- (146) Popov, A.; Kondratieva, E.; Goupil, J. M.; Mariey, L.; Bazin, P.; Gilson, J.-P.; Travert, A.; Maugé, F. Bio-Oils Hydrodeoxygenation:

- Adsorption of Phenolic Molecules on Oxidic Catalyst Supports. *J. Phys. Chem. C* **2010**, *114*, 15661–15670.
- (147) Nimmanwudipong, T.; Aydin, C.; Lu, J.; Runnebaum, R. C.; Brodwater, K. C.; Browning, N. D.; Block, D. E.; Gates, B. C. Selective Hydrodeoxygenation of Guaiacol Catalyzed by Platinum Supported on Magnesium Oxide. *Catal. Lett.* **2012**, *142*, 1190–1196.
- (148) Moghaddam, M. M.; Pieber, B.; Glasnov, T.; Kappe, C. O. Immobilized Iron Oxide Nanoparticles as Stable and Reusable Catalysts for Hydrazine-Mediated Nitro Reductions in Continuous Flow. *ChemSusChem* **2014**, *7*, 3122–3131.
- (149) Yao, H.; Wang, Y.; Jing, Y.; Luo, G. Ultrafast, Continuous and Shape-Controlled Preparation of CeO₂ Nanostructures: Nanorods and Nanocubes in a Microfluidic System. *Ind. Eng. Chem. Res.* **2018**, 57, 7525–7532.
- (150) Tao, S.; Yang, M.; Chen, H.; Zhao, S.; Chen, G. Continuous Synthesis of Ag/AgCl/ZnO Composites Using Flow Chemistry and Photocatalyic Application. *Ind. Eng. Chem. Res.* **2018**, *57*, 3263–3273.
- (151) Ma, J.; Tong, X.; Wang, J.; Zhang, G.; Lv, Y.; Zhu, Y.; Sun, S.; Yang, Y.-C.; Song, Y. Rare-Earth Metal Oxide Hybridized PtFe Nanocrystals Synthesized via Microfluidic Process for Enhanced Electrochemical Catalytic Performance. *Electrochim. Acta* **2019**, 299, 80–88.
- (152) Akram, M.; Razali, I. R.; Ghafoor, F.; Ur-Rahman, S.; Butt, F. K.; Hussain, R. Continuous Facile Synthesis of Nano-Sized Zinc Oxide and its Optical Properties. *Mater. Res. Express* **2018**, *5*, 075901.
- (153) Jiao, M.; Jing, L.; Wei, X.; Liu, C.; Luo, X.; Gao, M. The Yin and Yang of Coordinating Co-Solvents in the Size-Tuning of Fe₃O₄ Nanocrystals Through Flow Synthesis. *Nanoscale* **2017**, *9*, 18609–18612
- (154) Akram, M.; Alshemary, A. Z.; Butt, F. K.; Goh, Y.-F.; Ibrahim, W. A. W.; Hussain, R. Continuous Microwave Flow Synthesis and Characterization of Nanosized Tin Oxide. *Mater. Lett.* **2015**, *160*, 146–149.
- (155) Denis, C. J.; Tighe, C. J.; Gruar, R. I.; Makwana, N. M.; Darr, J. A. Nucleation and Growth of Cobalt Oxide Nanoparticles in a Continuous Hydrothermal Reactor under Laminar and Turbulent Flow. Cryst. Growth Des. 2015, 15, 4256–4265.
- (156) Cheung, T.-L.; Hong, L.; Rao, N.; Yang, C.; Wang, L.; Lai, W. J.; Chong, P. H. J.; Law, W.-C.; Yong, K.-T. The Non-Aqueous Synthesis of Shape Controllable Cu_{2-x}S Plasmonic Nanostructures in a Continuous-Flow Millifluidic Chip for the Generation of Photo-Induced Heating. *Nanoscale* **2016**, *8*, 6609–6622.
- (157) Kumar, V.; Fuster, H. A.; Oh, N.; Zhai, Y.; Deshpande, K.; Shim, M.; Kenis, P. J. A. Continuous Flow Synthesis of Anisotropic Cadmium Selenide and Zinc Selenide Nanoparticles. *Chem. Nano Mat* **2017**, *3*, 204–211.
- (158) Naughton, M. S.; Kumar, V.; Bonita, Y.; Deshpande, K.; Kenis, P. J. A. High Temperature Continuous Flow Synthesis of CdSe/CdS/ZnS, and CdSe/ZnS Nanocrystals. *Nanoscale* **2015**, *7*, 15895–15903.
- (159) Nightingale, A. M.; Bannock, J. H.; Krishnadasan, S. H.; O'Mahony, F. T. F.; Haque, S. A.; Sloan, J.; Drury, C.; McIntyre, R.; deMello, J. C. Large-Scale Synthesis of Nanocrystals in a Multichannel Droplet Reactor. *J. Mater. Chem. A* **2013**, *1*, 4067–4076.
- (160) Liang, X.; Baker, R. W.; Wu, K.; Deng, W.; Ferdani, D.; Kubiak, P. S.; Marken, F.; Torrente-Murciano, L.; Cameron, P. J. Continuous Low Temperature Synthesis of MAPbX₃ Perovskite Nanocrystals in a Flow Reactor. *React. Chem. Eng.* **2018**, *3*, 640–644.
- (161) Bezinge, L.; Maceiczyk, R. M.; Lignos, İ.; Kovalenko, M. V.; deMello, A. J. Pick a Color MARIA: Adaptive Sampling Enables the Rapid Identification of Complex Perovskite Nanocrystal Compositions with Defined Emission Characteristics. *ACS Appl. Mater. Interfaces* **2018**, *10*, 18869–18878.
- (162) Baek, J.; Allen, P. A.; Bawendi, M. G.; Jensen, K. F. Investigation of Indium Phosphide Nanocrystal Synthesis Using a High-Temperature and High-Pressure Continuous Flow Microreactor. *Angew. Chem., Int. Ed.* **2011**, *50*, 627–630.
- (163) Vikram, A.; Kumar, V.; Ramesh, U.; Balakrishnan, K.; Oh, N.; Deshpande, K.; Ewers, T.; Trefonas, P.; Shim, M.; Kenis, P. J. A. A

- Millifluidic Reactor System for Multistep Continuous Synthesis of InP/ZnSeS Nanoparticles. *Chem. Nano Mat* **2018**, *4*, 943–953.
- (164) Mora-Tamez, L.; Barim, G.; Downes, C.; Williamson, E. M.; Habas, S. E.; Brutchey, R. L. Controlled Design of Phase-and Size-Tunable Monodisperse Ni₂P Nanoparticles in a Phosphonium-Based Ionic Liquid through Surface Response Methodology. *Chem. Mater.* **2019**, *31*, 1552–1560.
- (165) Lignos, I.; Maceiczyk, R.; deMello, A. J. Microfluidic Technology: Uncovering the Mechanisms of Nanocrystal Nucleation and Growth. *Acc. Chem. Res.* **2017**, *50*, 1248–1257.
- (166) Bedard, A.-C.; Adamo, A.; Aroh, K. C.; Russell, M. G.; Bedermann, A. A.; Torosian, J.; Yue, B.; Jensen, K. F.; Jamison, T. F. Reconfigurable System for Automated Optimization of Diverse Chemical Reactions. *Science* **2018**, *361*, 1220–1225.
- (167) Rubens, M.; Vrijsen, J. H.; Laun, J.; Junkers, T. Precise Polymer Synthesis by Autonomous Self-Optimizing Flow Reactors. *Angew. Chem., Int. Ed.* **2019**, *58*, 3183–3187.
- (168) Krishnadasan, S.; Tovilla, J.; Vilar, R.; deMello, A. J.; deMello, J. C. On-Line Analysis of CdSe Nanoparticle Formation in a Continuous Flow Chip-Based Microreactor. *J. Mater. Chem.* **2004**, *14*, 2655–2660.
- (169) Lignos, I.; Protesescu, L.; Stavrakis, S.; Piveteau, L.; Speirs, M. J.; Loi, M. A.; Kovalenko, M. V.; deMello, A. J. Facile Droplet-Based Microfludic Synthesis of Monodisperse IV-VI Semiconductor Nanocrystals with Coupled In-Line NIR Fluorescence Detection. *Chem. Mater.* **2014**, 26, 2975–2982.
- (170) Polte, J.; Thunemann, A. F.; Sokolov, S.; Ahner, T. T.; Rademann, K.; Emmerling, F.; Kraehnert, R.; Erler, R. Nucleation and Growth of Gold Nanoparticles Studied via in situ Small Angle X-ray Scattering at Millisecond Time Resolution. *ACS Nano* **2010**, *4*, 1076—1082.
- (171) Karim, A. M.; Al Hasan, N.; Ivanov, S.; Siefert, S.; Kelly, R. T.; Hallfors, N. G.; Benavidez, A.; Kovarik, L.; Jenkins, A.; Winans, R. E.; Datye, A. K. Synthesis of 1 nm Pd Nanopartilces in a Microfluidic Reactor: Insights from in Situ X-ray Absorption Fine Structure Spectroscopy and Small-Angle X-ray Scattering. *J. Phys. Chem. C* **2015**, *119*, 13257–13267.
- (172) Niu, G.; Zhang, L.; Ruditskiy, A.; Wang, L.; Xia, Y. A Droplet-Reactor System Capable of Automation for the Continuous and Scalable Production of Noble-Metal Nanocrystals. *Nano Lett.* **2018**, 18, 3879–3884.
- (173) Sengul, H.; Theis, T. L.; Ghosh, S. Toward Sustainable Nanoparticles. *J. Ind. Ecol.* **2008**, *12*, 329–359.